Available online at www.sciencedirect.com

ScienceDirect

Underground Space 26 (2026) 412–434

www.keaipublishing.com/undsp

Research Paper

Optimization of shield tunnel joints: Focusing on structural performance with considerations for low-carbon emissions and economic efficiency

Minjin Cai [a], Timon Rabczuk [d], Shuwei Zhou [b,c], Xiaoying Zhuang [b,c,e,*]

[a] School of Civil Engineering, Fuzhou University, Fuzhou 350116, China
[b] Department of Geotechnical Engineering, College of Civil Engineering, Tongji University, Shanghai 200092, China
[c] State Key Laboratory for Disaster Reduction in Civil Engineering, Tongji University, Shanghai 200092, China
[d] Institute of Structural Mechanics, Bauhaus University of Weimar, Weimar 99423, Germany
[e] Computational Science and Simulation Technology, Faculty of Mathematics and Physics, Leibniz University Hannover, Hannover 30167, Germany

Received 10 September 2024; received in revised form 17 February 2025; accepted 20 February 2025
Available online 03 December 2025

Abstract

Optimizing shield tunnel joints is essential to meet the evolving demands of modern construction, where balancing structural performance, environmental impact, and cost efficiency is increasingly important. Traditional cast iron joint (CIJ) has been widely used, but there remains significant room for improvement in terms of both their mechanical efficiency and sustainability. This study addresses these challenges by investigating two alternative designs: the single row sleeve joint (SRSJ) and the double row sleeve joint (DRSJ). The research focuses on evaluating their mechanical performance and potential to reduce carbon emissions and costs, offering a more comprehensive and future-forward solution compared to the traditional CIJ. Through experimental testing, key performance factors such as joint deflection, rotational angle, concrete strain, and bolt strain were analyzed alongside joint toughness, ductility, cracking patterns, embodied carbon, and material cost. Key findings revealed that SRSJ achieved 97% of CIJ's ultimate bearing capacity, while DRSJ reached only 75%. In the elastic phase, SRSJ performed significantly better, supporting twice the load of CIJ. Bolt strain analysis showed that DRSJ experienced greater stress concentration, while SRSJ maintained balanced strain distribution. SRSJ also outperformed CIJ and DRSJ in toughness and ductility, particularly in rotational flexibility, exceeding CIJ by 76%. SRSJ and DRSJ all demonstrated lower embodied carbon and costs compared to CIJ, with reductions of up to 7.21% in emissions and 6.42% in costs. Overall, SRSJ emerged as a viable alternative, balancing mechanical performance, sustainability, and cost efficiency. In contrast, DRSJ's stress concentration issues limited its effectiveness, making it less advantageous compared to CIJ.

Keywords: Joint optimization; Shield tunnel; Structural performance; Sustainability

1 Introduction

Shield tunnels are crucial to modern infrastructure, especially in urban transportation and underground utility networks (Ouyang et al., 2024; Xu et al., 2024; C. Zhang et al., 2024). With accelerating urbanization, there is a growing demand for tunnel systems that are reliable and durable. A fundamental component of shield tunnels is the segmental joint, which connects tunnel segments to ensure structural stability and durability. These joints are designed to withstand high loads and maintain alignment between segments, directly influencing the tunnel system's performance. However, these joints are susceptible to failures such as cracking, joint opening, and deformation under prolonged stress or improper alignment, potentially

* Corresponding author at: Department of Geotechnical Engineering, College of Civil Engineering, Tongji University, Shanghai 200092, China.
E-mail address: xiaoyingzhuang@tongji.edu.cn (X. Zhuang).
Peer review under the responsibility of Tongji University

https://doi.org/10.1016/j.undsp.2025.02.012

compromising the structural integrity of the tunnel (Saleh et al., 2024; Y. Zhang et al., 2024; Z. Zhang et al., 2024b).

Segmental joints in shield tunnels are typically constructed from materials like cast iron, steel, and various reinforced composites, each offering distinct benefits and limitations. Cast iron joint (CIJ), for instance, has traditionally been the industry standard, known for its strength and durability (Al-Mansour et al., 2019; Alani et al., 2024; Cheng et al., 2024; Li et al., 2014; López et al., 2023). However, CIJ presents certain drawbacks, including high material costs and substantial environmental impact due to the energy-intensive production process. Additionally, CIJ has high embodied carbon, defined as the total greenhouse gas emissions from material extraction to manufacturing and construction, which adds to its environmental burden. CIJ is also heavy and challenging to handle, potentially slowing down construction and increasing labor costs, making them less economically viable in fast-paced construction environments (Marques et al., 2019; Tsiampousi et al., 2017; Ünal et al., 2024).

The growing emphasis on environmental sustainability and economic efficiency in construction has driven the search for alternative joint designs and materials that can balance structural integrity with low-carbon objectives and cost-effectiveness. Governments, contractors, and stakeholders are prioritizing solutions that reduce carbon emissions while maintaining performance standards (Al-Mansour et al., 2019; Alani et al., 2024; Cheng et al., 2024). Projects also face pressure to reduce costs and accelerate timelines without compromising safety or quality (Liew et al., 2017; Sivakrishna et al., 2020). Meeting these competing demands in shield tunnel joint design requires solutions that fulfill the criteria of high performance, low-carbon emissions, and economic efficiency (Lombardi et al., 2023; Rodríguez & Pérez, 2021; Song et al., 2024; Zhang et al., 2018).

In response, this study explores two new segment joint designs that incorporate efficient material distribution and alternative materials to reduce embodied carbon compared to CIJ. These designs aim to address the issues of cost, sustainability, and load-bearing performance essential for modern construction standards. While CIJ has been a reliable choice historically, the need for environmentally friendly and efficient practices underscores the importance of optimizing shield tunnel joints to meet the complex requirements of today's infrastructure projects. The potential exists to enhance material efficiency, lower carbon emissions, and streamline construction processes without sacrificing the necessary structural integrity of the tunnel (Assaad, 2024; Chen et al., 2024; Migunthanna et al., 2024; Z. Zhang et al., 2024a).

The main objective of this research is to optimize shield tunnel joints by balancing structural performance, environmental sustainability, and economic viability. This study compares CIJ with two new joint designs, focusing on performance metrics such as load-bearing capacity, rotational flexibility, deflection, and crack resistance. Experimental testing evaluates the behavior of each joint type under typical tunnel loading conditions. Additionally, the study assesses the embodied carbon and cost efficiency of each joint design, providing a comprehensive view of their sustainability and economic benefits.

The paper is organized as follows: The experimental results section discusses joint deflection, joint opening, rotational angle, concrete strain, and bolt strain for the three joint types. A subsequent discussion examines joint toughness, ductility, cracking patterns, and sustainability aspects. The paper concludes with key insights and recommendations for optimizing future tunnel joint designs to meet modern construction demands.

2 Experimental preparation

2.1 Joint design

Figure 1 illustrates the dimensional characteristics of the CIJ, single row sleeve joint (SRSJ), and double row sleeve joint (DRSJ), which reflect their distinct design philosophies and intended applications in shield tunnel construction, with notable differences in weight that highlight their material efficiency and suitability for various load conditions. The CIJ, with its traditional and robust design, features a substantial width of approximately 35.78 mm and a height of 28.78 mm. Its significant cross-sectional thickness, particularly around the anchoring points, underscores its high capacity for load-bearing and resistance to deformation, making it ideal for heavy-duty applications where durability is paramount. However, this robust construction results in a considerable weight of 31.86 kg, which complicates installation and increases material costs.

In contrast, the single row sleeve joint adopts a more streamlined approach, with dimensions of 458 mm in length and 144 mm in width, significantly reducing material usage and resulting in a weight of only 9.96 kg. This represents a weight reduction of approximately 68.7% compared to the CIJ. This substantial decrease in weight simplifies handling and installation, and it improves material efficiency without compromising the joint's ability to provide adequate support in moderate load scenarios. The elongated form and thinner walls indicate a focus on optimizing material distribution to achieve sufficient structural integrity while minimizing unnecessary bulk.

The DRSJ, while maintaining similar overall dimensions to the single row version, introduces a dual-row configuration intended to enhance stress distribution across the joint. Despite this additional complexity, the DRSJ weighs just 9.12 kg, making it the lightest among the three. This represents a reduction in weight of about 71.4% compared to the CIJ. The slight reduction in thickness in certain areas may limit its strength under very high loads, suggesting the need for further testing to validate its load-bearing capabilities fully. However, the weight savings and the improved

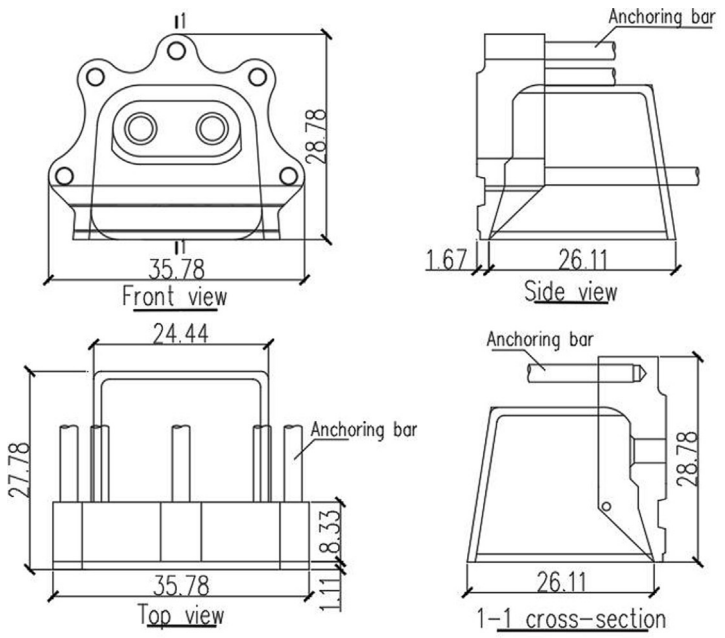

(a)

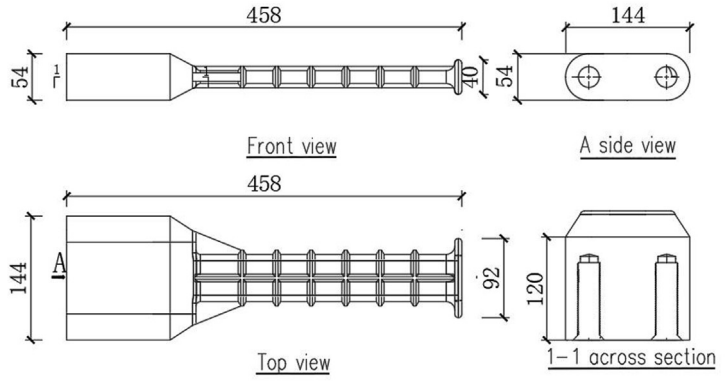

(b)

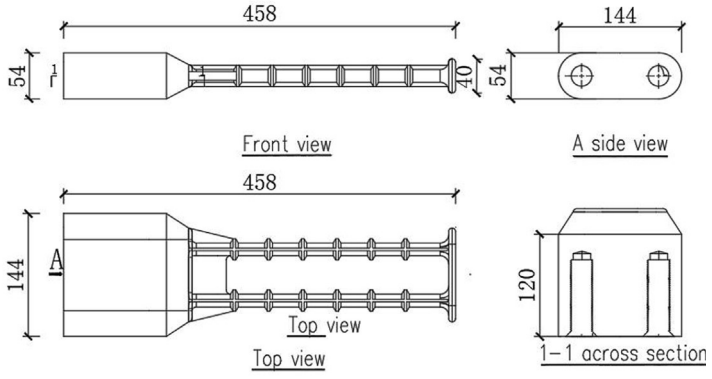

(c)

Fig. 1. Dimensions of shield tunnel joints. (a) Cast iron joint, (b) single row sleeve joint, and (c) double row sleeve joint. (Unit: mm)

potential for stress distribution highlight the careful balance between size, weight, and structural performance. Overall, these joints demonstrate the trade-offs between strength, material efficiency, and application-specific performance, with the weight differences illustrating the significant advancements in design efficiency and construction feasibility.

2.2 Material preparation

The mixture proportions for all three joint types were kept consistent to ensure that any differences in performance were attributed to the joint type rather than variations in the concrete mixture. The mixture proportions are detailed in Table 1. For each joint type, the mix consisted of cement, water, fly ash, slag, fine sand, coarse aggregate, and admixtures in consistent ratios. Specifically, the mass ratio of cement to water was set at 1:0.38, with fly ash and slag each comprising 13% of the cement content. Fine sand and coarse aggregate were added at proportions of 2.04 and 3.06 times the cement content, respectively. A small percentage of admixture (0.02) was included to enhance the concrete's workability. The joint types, being the primary variable, were cast iron for the CIJ, a single row sleeve for the SRSJ, and a double row sleeve for the DRSJ.

2.3 Segmental preparation

Figure 2 provides a comprehensive overview of the construction stages involved in the fabrication of shield tunnel joints, illustrating the critical steps from initial mold setup to the final curing of the concrete. The sequence began with mold preparation and surface treatment (Fig. 2(a)), ensuring that the mold was properly conditioned for the subsequent steps. The positioning of the CIJ and rebar (Fig. 2(b)) was crucial for establishing the structural integrity required for the tunnel joints. This was followed by the placement of the SRSJ with rebar (Fig. 2(c)) and the assembly of the DRSJ with rebar (Fig. 2(d)). All three joint types were cast from iron. The concrete was subsequently poured around them to form the segmental units needed for load testing, as shown in later stages of Fig. 2. This pouring process (Fig. 2(e)) ensured even distribution and compaction within the mold. After the initial setting of the concrete, steam curing (Fig. 2(f)) was applied to accelerate hardening and improve material properties. Once the concrete had set, the formwork was removed (Fig. 2(g)), revealing the partially finished joint segment. The final stage involved outdoor curing of the concrete (Fig. 2(h)), allowing the joint segment to achieve the desired strength and durability through natural curing.

2.4 Experimental set up

Figure 3 illustrates the detailed experimental setup used to evaluate the structural performance of shield tunnel segment joints. The test was conducted with a comprehensive system designed to simulate real-world tunnel conditions, enabling accurate measurements of various factors influencing joint behavior under load. The setup included a loading system that applied a controlled vertical force to the segment joint, simulating the compressive loads experienced in actual tunnels. The bending test loading points were spaced 80 cm apart to replicate actual bending stress conditions on the tunnel segments. This load was applied incrementally, with the data acquisition system capturing measurements at a frequency of once per second to ensure detailed tracking of joint response throughout each load increment. A control system regulated the load application to maintain consistency. To monitor material strain as the load increased, concrete strain gauges were strategically attached to the concrete surface, providing insights into stress distribution around the joint. Linear variable differential transformers (LVDTs) were used to measure key deformations: one LVDT tracked joint opening, and another recorded deflection. Additionally, bolt strain gauges were placed on high-strength bolts at critical points, measuring stress on the bolts connecting the segment and contributing to a complete assessment of joint performance.

Figure 4 shows the layout of measurement points and loading point. Concrete strain gauges were placed on the lower surface of the specimen (MD-1 to MD-6), while bolt strain gauges (BS1 to BS8) were positioned on the bolts. LVDTs were mounted at strategic points (LO-1, LO-2, UO-1, UO-2, and LVDT 1 to 6) to measure both joint opening and deflection. The loading points were applied symmetrically across the specimen, as shown in Fig. 5(b), ensuring a balanced distribution of load. By monitoring joint opening, deflection, concrete strain, and bolt strain, the system enables a thorough analysis of the structural integrity and load-bearing capacity of the tested joints, contributing to a better understanding of their behavior under high loads.

Table 1
Mixture proportion.

Joint type	Cement	Water	Fly ash	Slag	Fine sand	Coarse aggregate	Admixture
Cast iron joint	1.00	0.38	0.13	0.13	2.04	3.06	0.02
Single row sleeve joint	1.00	0.38	0.13	0.13	2.04	3.06	0.02
Double row sleeve joint	1.00	0.38	0.13	0.13	2.04	3.06	0.02

Fig. 2. Construction stages of shield tunnel joints: (a) mold setup and surface preparation, (b) placement of CIJ and rebar, (c) placement of SRSJ with rebar, (d) assembly of DRSJ and rebar, (e) concrete pouring operation, (f) steam curing after initial set, (g) formwork removal process, and (h) final curing of concrete outdoors.

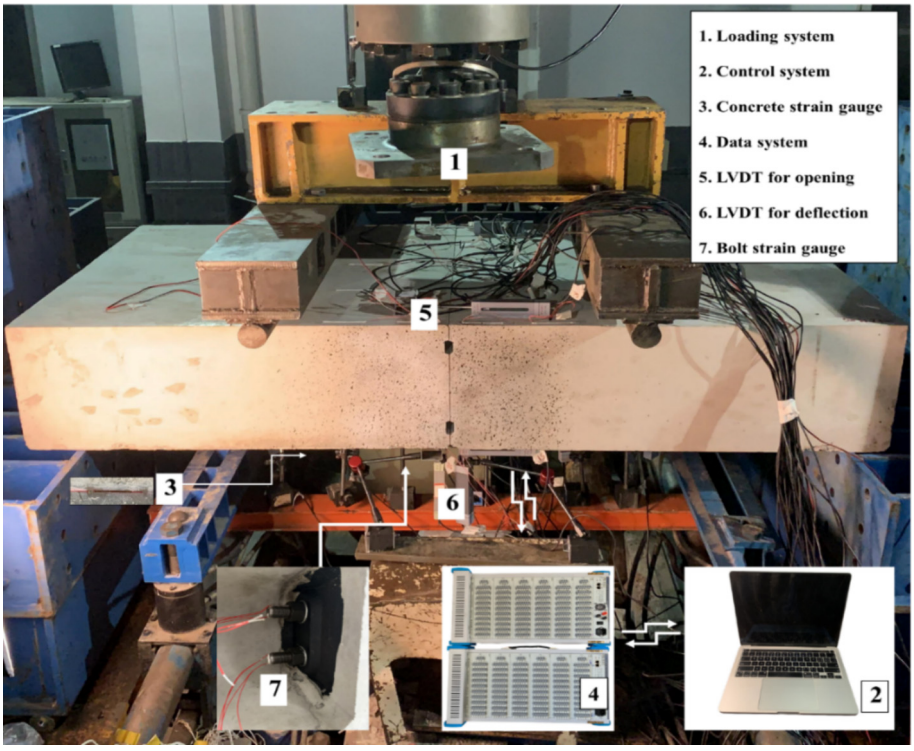

Fig. 3. Experimental system.

3 Experimental results

Figure 5 illustrates the global response of the three different joint types (CIJ, SRSJ, and DRSJ) under various load conditions, focusing on bearing capacity, deflection, joint opening, and joint rotational angle. The data presented covers the three key phases of the joint's behavior: elastic phase (F_{cr}), plastic stable phase (F_{psp}), and plastic accelerated phase (F_{pap}). These phases were identified based on the load-joint deflection and load-joint rotation curves observed during testing. Specifically, the elastic phase was defined as the stage where deformation occurs without any cracking, maintaining an approximately linear relationship between load and joint deflection/rotation. The plastic stable phase was marked by the initiation of cracking, with crack development progressing at a steady rate and showing minimal increases in joint deflection despite increasing load. Finally, the plastic accelerated phase was identified as the point where joint deflection or rotation began to increase rapidly with additional load, accompanied by an accelerated rate of crack growth, signaling significant plastic deformation. In the elastic phase, SRSJ reaches about 200% of the bearing capacity of CIJ, while DRSJ achieves 123%. In the plastic stable phase, SRSJ achieves approximately 114% of CIJ's capacity, and DRSJ reaches about 96%. Finally, in the plastic accelerated phase, SRSJ achieves around 97% of the CIJ capacity, while DRSJ is notably lower, at about 75%. These comparisons demonstrate that while SRSJ performs comparably to CIJ, DRSJ shows a significant reduction in

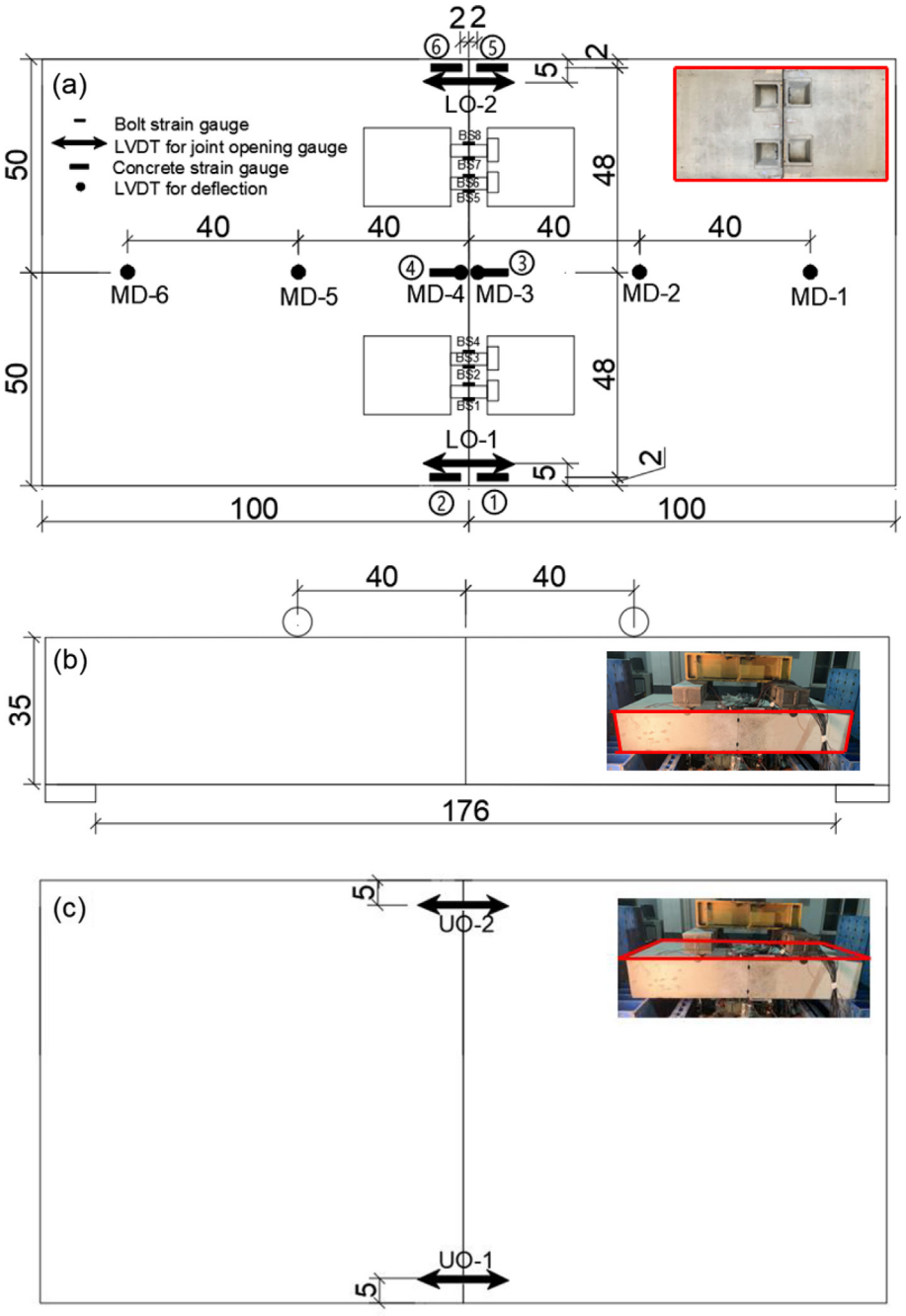

Fig. 4. Layout of measurement points and loading point. (a) Lower surface, (b) latter surface, and (c) upper surface. (Unit: mm)

the plastic accelerated phase, reflecting its lower load-bearing capacity. These preliminary observations highlight the varying structural responses between the joint types, suggesting different applications and performance characteristics. Detailed analysis of each parameter is provided in the subsequent sections.

3.1 Joint deflection

Figures 6–8 illustrate the relationships between load and deflection and the increments in deflection under increasing load conditions (Cai et al., 2024a, 2024b). Deflection increments here represent the increase in deflection corresponding to every 10 kN increment in load. Figure 6(a) shows the load–deflection relationship for the CIJ, revealing a three-stage behavior under increasing load: elastic phase, plastic stable phase, and plastic accelerated phase. The circled numbers correspond to the three phases of joint behavior. These markings help to visually indicate the points in the load–deflection and load-rotation curves where each phase occurs, providing a clear reference to the progression of joint behavior under load conditions. The elastic phase extended from 0 to 130 kN, corresponding to a deflection of 1.90 mm. This was followed by a stable plastic phase

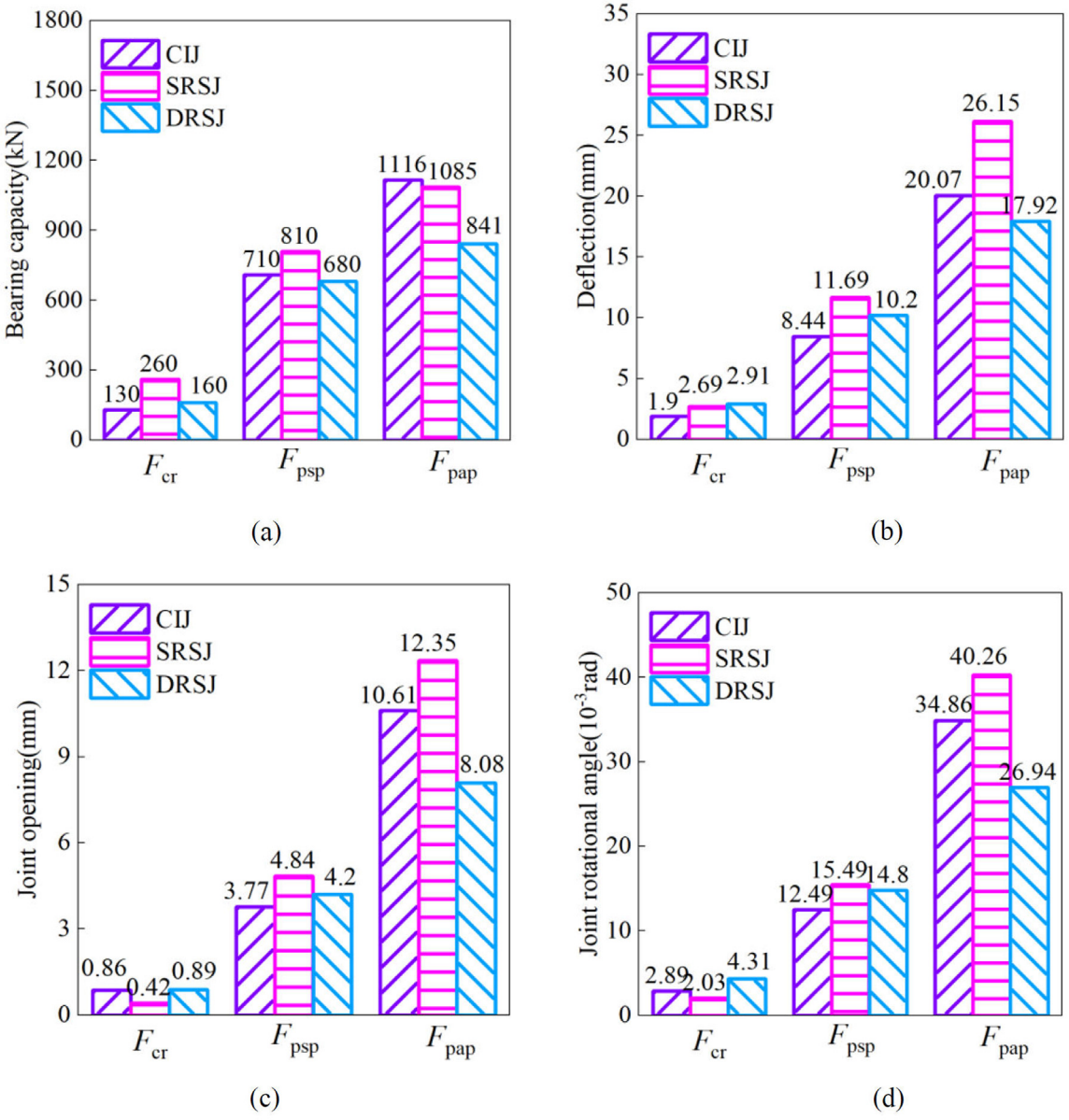

Fig. 5. Global response. (a) Bearing capacity, (b) deflection, (c) joint opening, and (d) joint rotational angle. F_{cr} corresponds to the elastic phase; F_{psp} corresponds to the plastic stable phase; F_{pap} corresponds to the plastic accelerated phase.

extending from 130 to 710 kN, with a deflection of 8.44 mm. Finally, the plastic accelerated phase began at 710 kN and peaked at a load of 1 116 kN, with a deflection of 20.07 mm. The lengths of these phases were 130 kN for the elastic phase, 580 kN for the plastic stable phase, and 406 kN for the plastic accelerated phase. In Fig. 6(b), the deflection increments for the CIJ are shown. During the elastic phase, the maximum deflection increment was 0.11 mm. As the joint transitioned to the plastic stable phase, the maximum deflection increment increased to 0.27 mm, representing a 145.5% increase compared to the elastic phase. In the plastic accelerated phase, the maximum increment reached 0.63 mm, a 133.3% increase compared to the plastic stable phase. The phase lengths suggest that the CIJ underwent a long and stable plastic phase, allowing it to bear loads steadily before reaching its failure point in the plastic accelerated phase.

Figure 7 illustrates the load–deflection behavior for the SRSJ. Compared to the CIJ, the elastic phase extended up to 260 kN, corresponding to a deflection of 2.69 mm. This represented a 100% increase in phase length compared to the CIJ. The stable plastic phase occurred between 260 and 810 kN, covering a load range of 550 kN and corresponding to a deflection of 11.69 mm. The plastic accelerated phase then occurred between 810 and 1 085 kN, covering a shorter range of 275 kN, with a final deflection of 26.15 mm. Compared to the CIJ, SRSJ had a 100% longer elastic phase but a slightly shorter plastic stable phase by about 5.2%. However, the plastic accelerated phase was also shorter by 32.3%, indicating a quicker

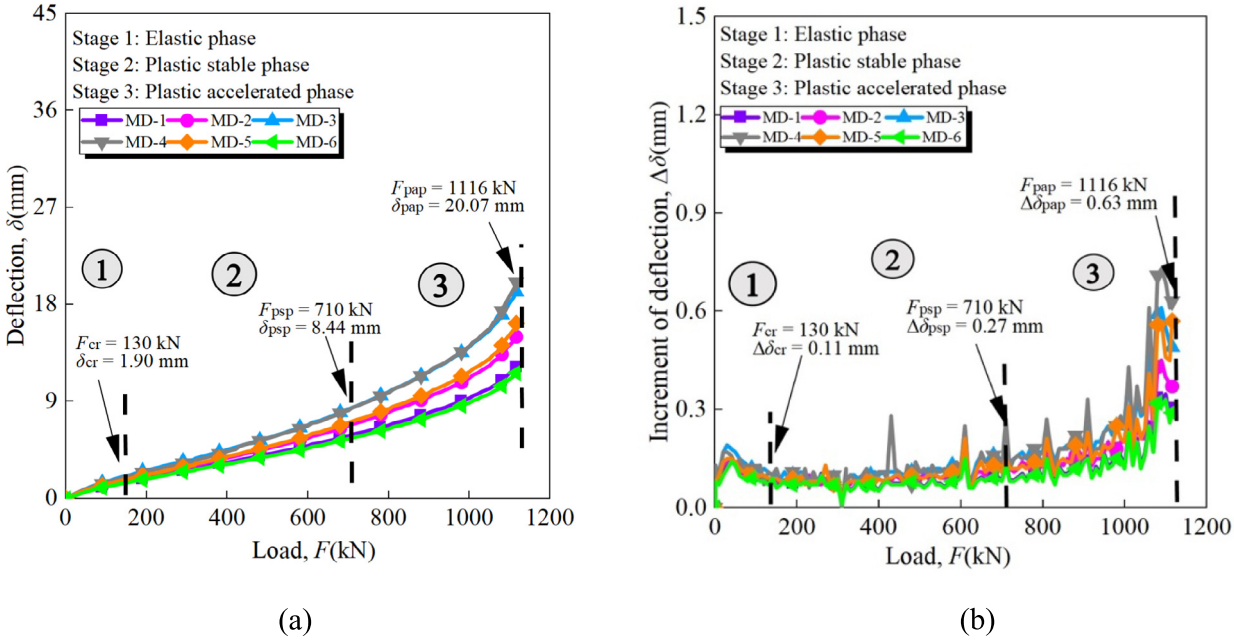

Fig. 6. Deflection properties of CIJ. (a) Load-deflection relationships, and (b) load–deflection increment relationships.

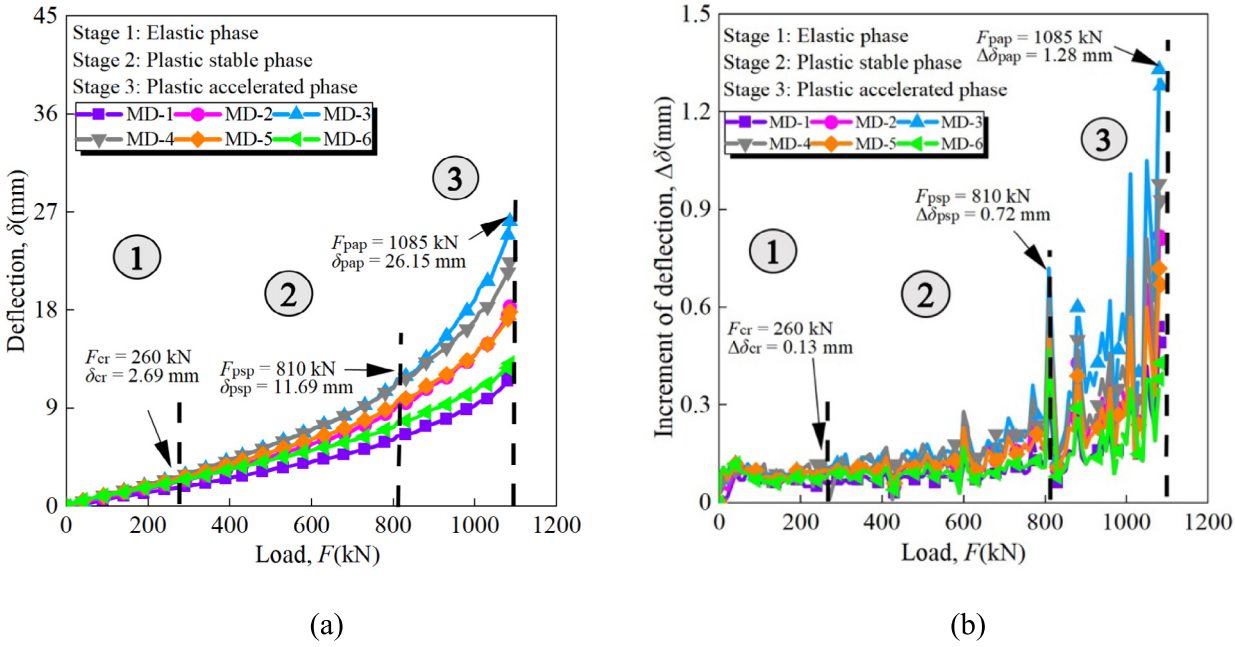

Fig. 7. Deflection properties of SRSJ. (a) Load-deflection relationships, and (b) load–deflection increment relationships.

transition to failure. In Fig. 7(b), the deflection increments for the SRSJ show a more significant variation. In the elastic phase, the maximum deflection increment was 0.13 mm, which was slightly higher than that of the CIJ. During the plastic stable phase, the maximum deflection increment rose sharply to 0.72 mm, representing a 453.8% increase compared to the elastic phase. In the plastic accelerated phase, the maximum deflection increment reached 1.33 mm, an 84.7% increase compared to the plastic stable phase. These values indicate that the SRSJ, despite its simplified structure, maintains a relatively high level of load-bearing capacity and exhibits greater deformability. It performs comparably to the CIJ, achieving around 95% of the CIJ's load-bearing capacity, making it a feasible alternative for applications requiring high deformation tolerance while simplifying the structural design.

The analysis of the DRSJ, as shown in Fig. 8(a) and (b), reveals significant shortcomings. The load–deflection curve

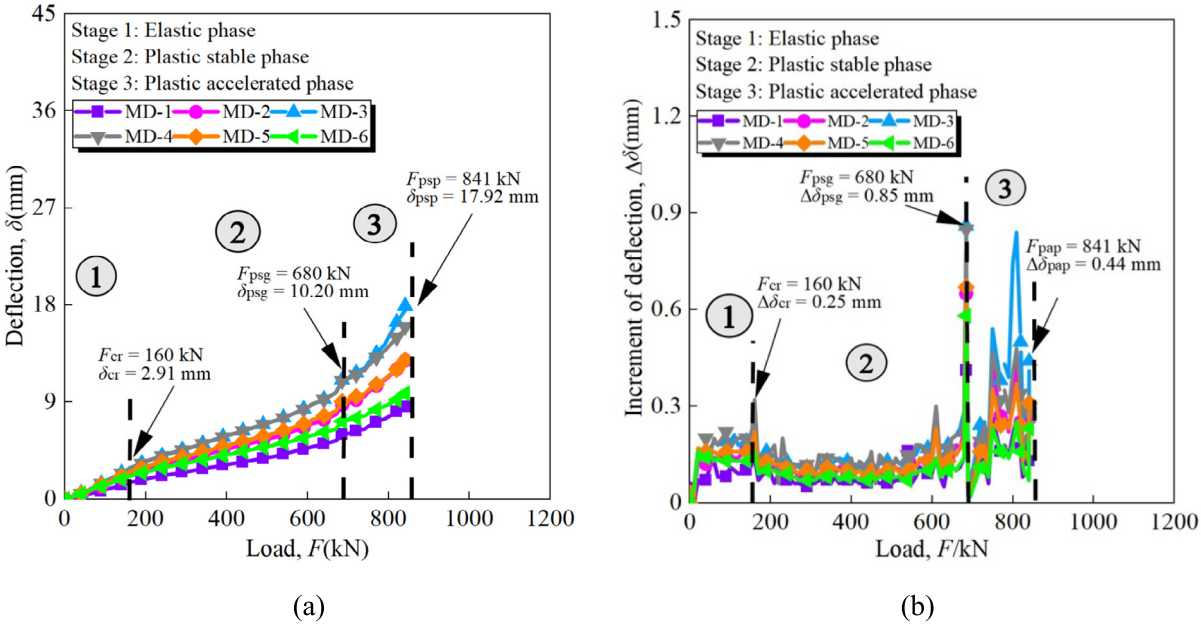

Fig. 8. Deflection properties of DRSJ. (a) Load-deflection relationships, and (b) load–deflection increment relationships.

in Fig. 8(a) exhibits a similar three-stage behavior but with different phase lengths. The elastic phase extended up to 160 kN, corresponding to a deflection of 2.91 mm. This phase length was 23.1% longer than that of the CIJ but 38.5% shorter than the SRSJ. The plastic stable phase extended from 160 to 680 kN, covering a load range of 520 kN and corresponding to a deflection of 10.20 mm. This phase was 10.3% shorter than the CIJ and 5.5% shorter than the SRSJ. The plastic accelerated phase occurred between 680 and 841 kN, covering a load range of 161 kN, with a final deflection of 17.92 mm. This phase was significantly shorter by 60.3% compared to the CIJ and 41.5% shorter compared to the SRSJ, indicating that the DRSJ transitions more quickly to failure under high loads. The deflection increments for the DRSJ, as shown in Fig. 8 (b), also highlight its weaknesses. In the elastic phase, the maximum deflection increment was 0.32 mm, which was significantly higher than both the CIJ and the SRSJ, indicating that the joint experienced greater deformation even at lower loads. During the plastic stable phase, the maximum deflection increment was 0.28 mm, which was a 12.5% decrease compared to the elastic phase. However, this phase length was shorter, and the deflection increments were still relatively high, suggesting that the joint did not maintain its structural integrity as effectively as expected. In the plastic accelerated phase, the maximum deflection increment reached 0.84 mm, a 200% increase compared to the plastic stable phase. This rapid increase in deflection increment, combined with the shorter phase lengths, suggests that the DRSJ is prone to earlier failure and is less effective at distributing the load compared to the other joint types.

The DRSJ, contrary to expectations, does not perform as well as the CIJ or SRSJ. The data show that this joint enters failure stages more quickly, with shorter phase lengths in both the plastic stable and plastic accelerated phases. The larger deflection increments in the elastic phase indicate that the joint deforms more under load, which could lead to premature failure. This performance may be due to a design flaw, where the dual-row configuration, instead of providing better stress distribution, may create points of weakness or concentration of forces that reduce the overall effectiveness of the joint. Additionally, the rapid progression through the plastic phases suggests that the joint material or design does not adequately accommodate increasing loads, leading to early failure. Therefore, the current design of the DRSJ may not be suitable for applications requiring high load-bearing capacity and durability. In contrast, the SRSJ, despite its simplified structure, shows promising results. It maintains a load-bearing capacity that is approximately 95% of that of the CIJ, while exhibiting higher deformability. This performance highlights its potential as a viable alternative to the CIJ, especially in applications where reduced complexity and improved deformation tolerance are beneficial. The SRSJ demonstrates that it achieves comparable load-bearing performance with a more streamlined design, offering a balanced advantage in terms of economic cost, efficiency, and structural performance. This makes it a suitable option for various construction scenarios where a combination of reduced complexity, cost-effectiveness, and high deformation tolerance is crucial.

3.2 Joint opening

Figures 9–11 provide the joint opening properties of the CIJ, SRSJ, and DRSJ. The joint opening increments refer to the increase in joint opening corresponding to every

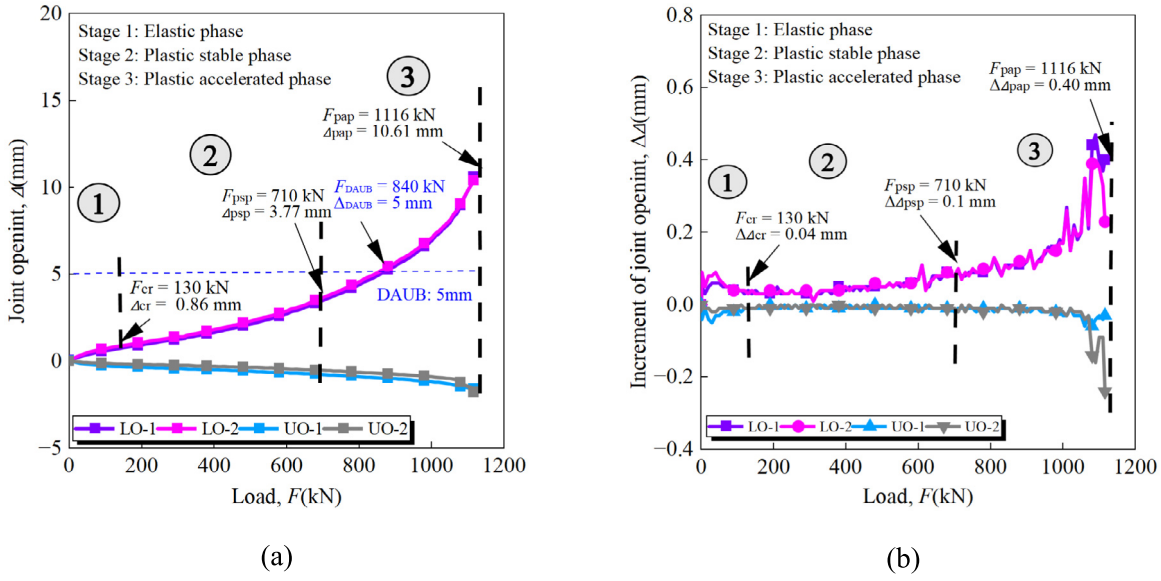

Fig. 9. Opening properties of CIJ. (a) Load-joint opening relationships, and (b) load-joint opening increment relationships.

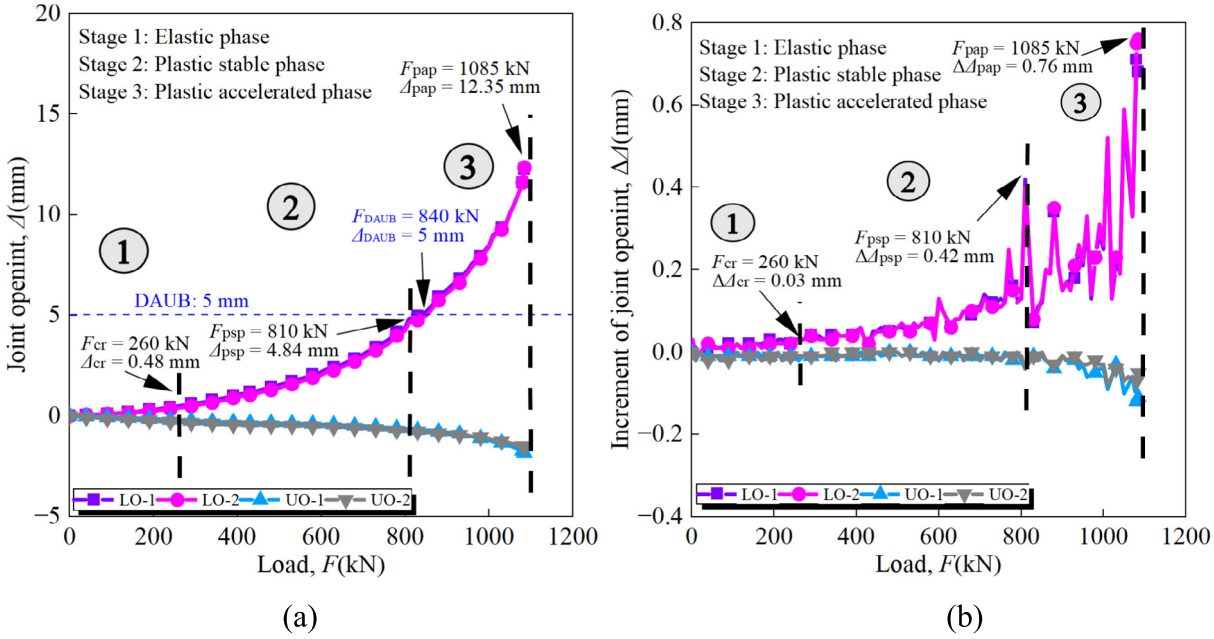

Fig. 10. Opening properties of SRSJ. (a) Load-joint opening relationships, and (b) load-joint opening increment relationships.

10 kN increment in load (Cai et al., 2024a, 2024b). The CIJ, as shown in Fig. 9(a), exhibited a relatively controlled joint opening behavior throughout the three stages: elastic phase, plastic stable phase, and plastic accelerated phase. In the initial elastic phase, the joint opening was minimal, with the maximum value reaching 0.86 mm. As the joint progressed into the plastic stable phase, the joint opening increased to 3.77 mm, representing a 338.4% increase from the elastic phase. Finally, in the plastic accelerated phase, the joint opening reached its peak value of 10.61 mm at the end of the test, a further increase of 181.4% from the plastic stable phase. This gradual increase in joint opening across the stages indicates that the CIJ maintains stable performance until the plastic accelerated phase, where the opening becomes more pronounced. Figure 9(b) shows the increments in joint opening for the CIJ. During the elastic phase, the maximum opening increment was 0.04 mm. As the joint transitioned to the plastic stable phase, the maximum opening increment increased to 0.10 mm, representing a 150% rise. In the plastic accelerated phase, the increment reached 0.40 mm, which was a 300% increase from the plastic stable phase. Compared to

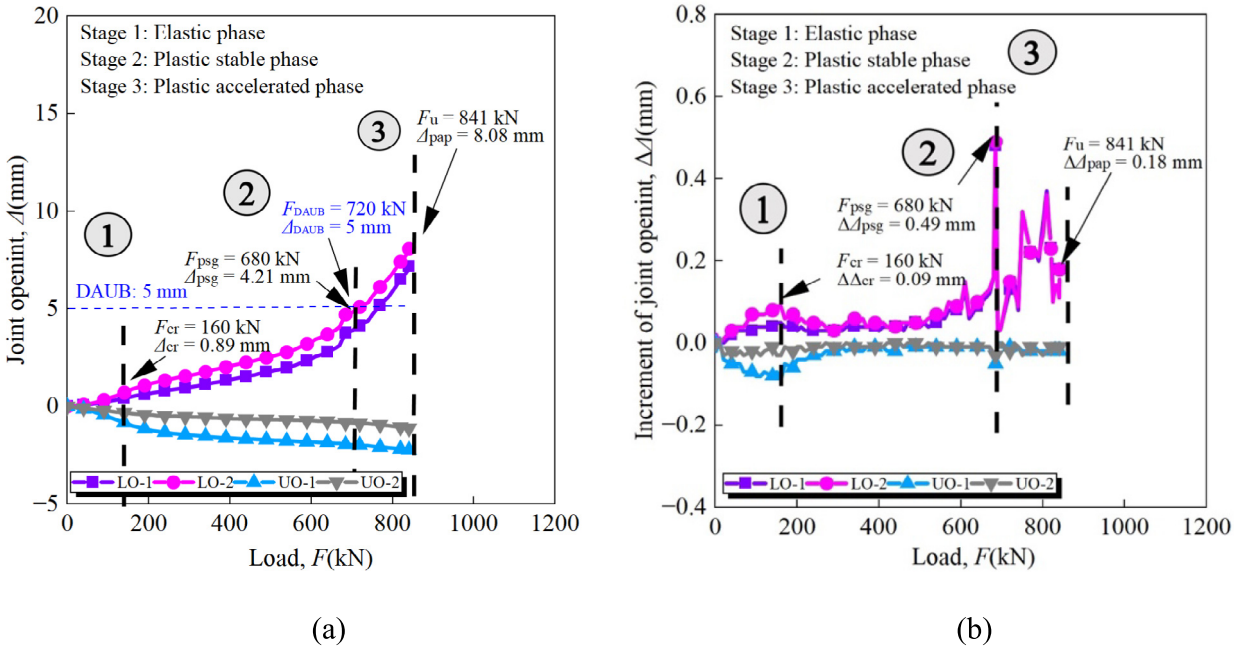

Fig. 11. Opening properties of DRSJ. (a) Load-joint opening relationships, and (b) load-joint opening increment relationships.

the other joint types, CIJ's joint opening increments remained relatively small, reflecting a controlled and gradual response to increasing load.

The SRSJ, illustrated in Fig. 10(a), showed a different joint opening profile compared to the CIJ. In the elastic phase, the joint opening remained low at 0.48 mm, which was 44.2% lower than the CIJ's elastic phase opening. However, as the joint entered the plastic stable phase, the joint opening increased more rapidly to 4.84 mm, representing a 908.3% increase from the elastic phase and a 28.4% increase over the CIJ's corresponding phase. In the plastic accelerated phase, the joint opening reached 12.35 mm, representing an increase of 155.1% from the plastic stable phase and an additional 16.4% over the CIJ's peak opening. This data suggests that while the SRSJ maintains stable performance in the early phase, it allows for more joint movement as the load increases, which could be beneficial in applications where flexibility is required. Figure 10(b) displays the increments in joint opening for the SRSJ. During the elastic phase, the maximum opening increment was 0.03 mm (25% lower than the CIJ's 0.04 mm). However, during the plastic stable phase, the maximum opening increment rose sharply to 0.42 mm (1300% increase from the elastic phase and 320% higher than the CIJ's 0.10 mm). In the plastic accelerated phase, the maximum opening increment reached 0.76 mm, which represented an 81% increase from the plastic stable phase and was 90% higher than the CIJ's 0.40 mm increment. Compared to the CIJ, the SRSJ shows a greater capacity for deformation in the later phases, with its increments rising more sharply, reflecting its flexibility under load.

The DRSJ, depicted in Fig. 11(a), exhibited the most pronounced joint opening behavior among the three joint types. In the elastic phase, the joint opening started at 0.89 mm (103.5% higher than the CIJ's 0.86 mm and 85.4% higher than the SRSJ's 0.48 mm). As the joint entered the plastic stable phase, the joint opening increased significantly to 5.21 mm (485.4% increase from the elastic phase and 38.2% higher than the SRSJ's 4.84 mm). In the plastic accelerated phase, the joint opening reached a maximum of 17.92 mm, representing a 244% increase from the plastic stable phase and 68.9% higher than the SRSJ's 12.35 mm. This extensive joint opening suggests that the DRSJ is more susceptible to large deformations, which may lead to earlier failure. Figure 11(b) illustrates the increments in joint opening for the DRSJ. During the elastic phase, the maximum opening increment was 0.09 mm (125% higher than the CIJ's 0.04 mm and 200% higher than the SRSJ's 0.03 mm). However, during the plastic stable phase, the maximum opening increment only slightly increased to 0.16 mm, representing a 77.8% rise and remaining 60% lower than the SRSJ's 0.42 mm in the same phase. In the plastic accelerated phase, the maximum opening increment reached 0.37 mm (131.3% increase from the plastic stable phase but still 51.3% lower than the SRSJ's 0.76 mm increment). This indicates that while the DRSJ does experience substantial joint opening, the increments are more moderate, reflecting a somewhat more controlled response in this final phase, but still leading to larger overall deformations.

According to the German standard (DAUB, 2013), a joint opening of 5 mm is a critical indicator of load-bearing capacity. The CIJ and SRSJ both reach 5 mm opening at approximately 840 kN, indicating similar performance. In contrast, the DRSJ reaches the 5 mm opening at 720 kN, which is approximately 14.3% lower than the

load required for the CIJ and SRSJ. This suggests that the DRSJ has a reduced load-bearing capacity, deforming more easily under similar loads compared to the CIJ and SRSJ.

The joint opening behavior and increments across the three joints reveal significant differences in their structural responses. The CIJ demonstrates a controlled and gradual increase in joint opening, with relatively small increments across all phases. This suggests a more stable response to increasing loads, making it suitable for applications where minimal joint movement is crucial. The SRSJ, on the other hand, shows greater flexibility, with a more significant rise in joint opening increments, particularly in the plastic stable and accelerated phases. This characteristic might be advantageous in scenarios where a higher tolerance for joint movement is needed. The DRSJ, while showing the highest overall joint openings, has more moderate increments, especially in the critical plastic accelerated phase. However, its larger overall joint movement suggests it may be prone to earlier failure, particularly in high-stress environments.

3.3 Joint rotational angle

Figure 12 provides an analysis of the joint rotational angle properties for CIJ, SRSJ, and DRSJ under increasing load conditions, focusing on the differences in their rotational behavior across three distinct relative trend stages. In the first stage (marked as 1), at a lower load level around 100 kN, the rotational angles for CIJ, SRSJ, and DRSJ are relatively close, reflecting similar stiffness and resistance to rotational movement. Notably, SRSJ exhibits the smallest rotational angle, indicating higher stiffness compared to CIJ and DRSJ, with DRSJ showing slightly higher flexibility. As the load increases into the second stage (marked as 2), the differences in rotational behavior become more pronounced. SRSJ continues to show the smallest rotational angle among the three joints, maintaining its rigidity under the increasing load. CIJ follows with a moderate rotational angle, while DRSJ displays the highest rotational angle, indicating that it allows for more rotational movement under the same load. This suggests that SRSJ retains a more controlled response, while DRSJ becomes more flexible, leading to greater rotational deformation. In the third stage (marked as 3), as the load continues to increase, a significant shift occurs. SRSJ, which initially exhibited the smallest rotational angles, gradually accelerates in its rotational angle growth and eventually surpasses CIJ. This shift indicates that while SRSJ initially maintained higher stiffness, it becomes more flexible under higher loads, allowing for greater rotation. Under the same load conditions, DRSJ consistently shows the highest rotational angle, reflecting its tendency toward greater deformation. CIJ, despite being surpassed by SRSJ in this stage, still maintains a relatively rigid profile compared to DRSJ.

Overall, the analysis across these stages reveals distinct trends: SRSJ starts as the most rigid joint but becomes more flexible as loads increase, eventually allowing more rotation than CIJ in the highest load conditions. Under the same load conditions, DRSJ consistently shows the greatest rotational movement, indicating potential for higher deformation and earlier structural compromise. CIJ, while less flexible than SRSJ in the later stages, still offers a more rigid and stable response throughout the loading process.

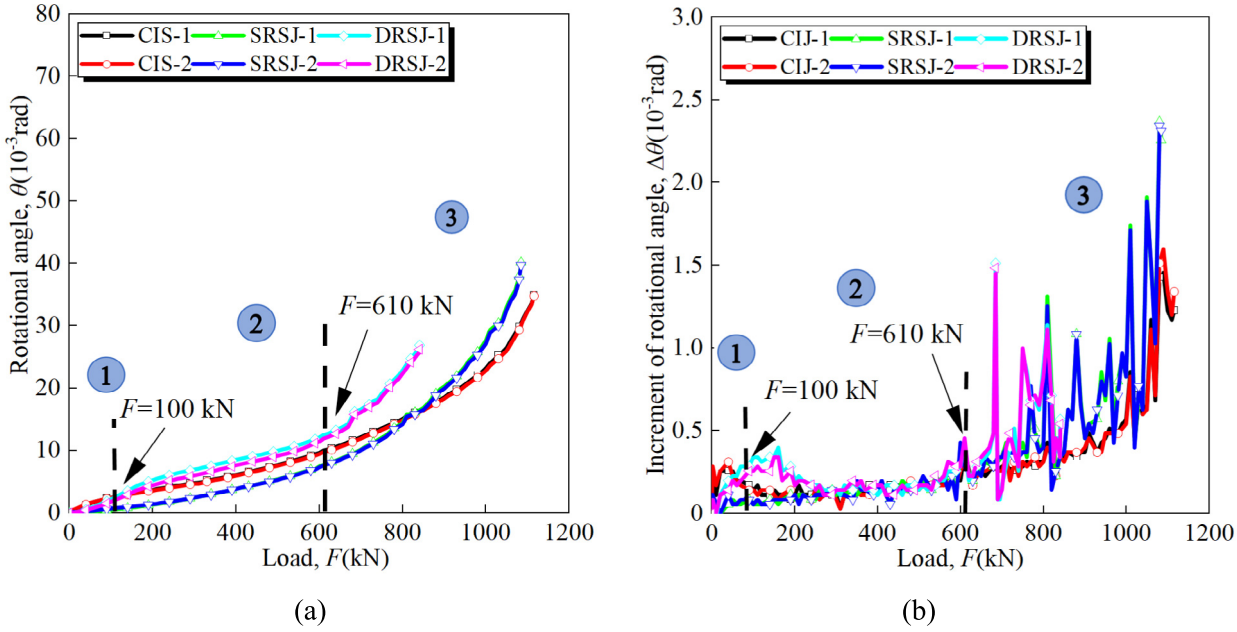

Fig. 12. Joint rotational angle properties. (a) Load-joint rotational angle relationships, and (b) load-joint rotational angle increment relationships.

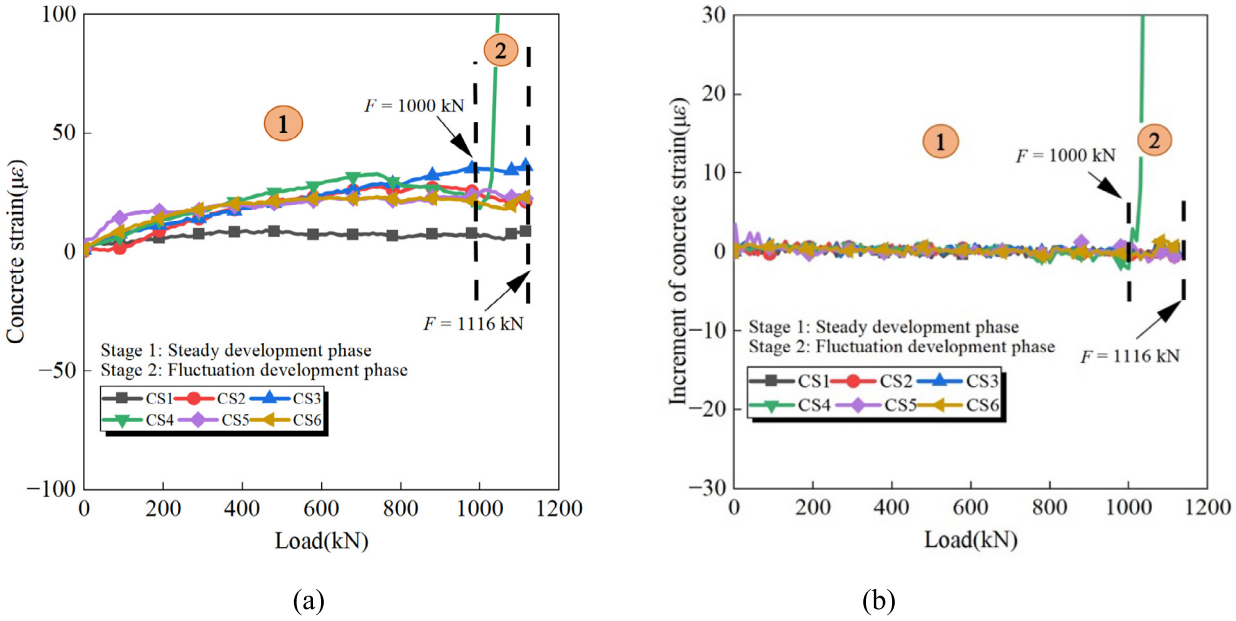

Fig. 13. Concrete strain properties of CIJ in the bottom face. (a) Load-concrete strain relationships, and (b) load-concrete strain increment relationships.

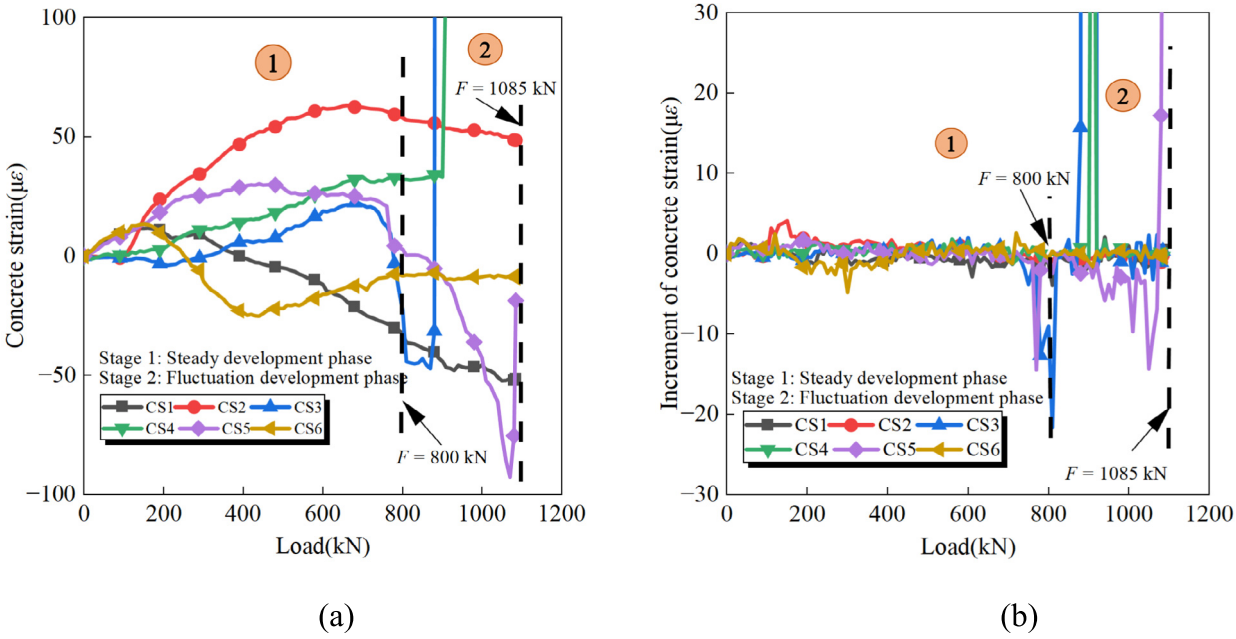

Fig. 14. Concrete strain properties of SRSJ in bottom face. (a) Load-concrete strain relationships, and (b) load-concrete strain increment relationships.

3.4 Concrete strain

Figures 13–15 provide an analysis of the concrete strain properties at the bottom face of CIJ, SRSJ, and DRSJ under increasing load conditions. These figures specifically examine the relationships between load and concrete strain, as well as the corresponding increments in concrete strain as the load increases.

In Fig. 13(a), the load-concrete strain relationship for the CIJ showed a two-stage behavior. During the first stage, identified as the steady development phase, the concrete strain remained relatively stable, with only slight increases as the load approached 1000 kN. This phase indicates that the CIJ maintains its structural integrity and effectively resists strain under increasing load. As the load surpassed 1000 kN and entered the second stage, labeled as the fluctuation development phase, the strain started to fluctuate more noticeably, particularly as it neared 1116 kN. Figure 13(b) illustrates that the increments in concrete strain for the CIJ were minimal during the steady

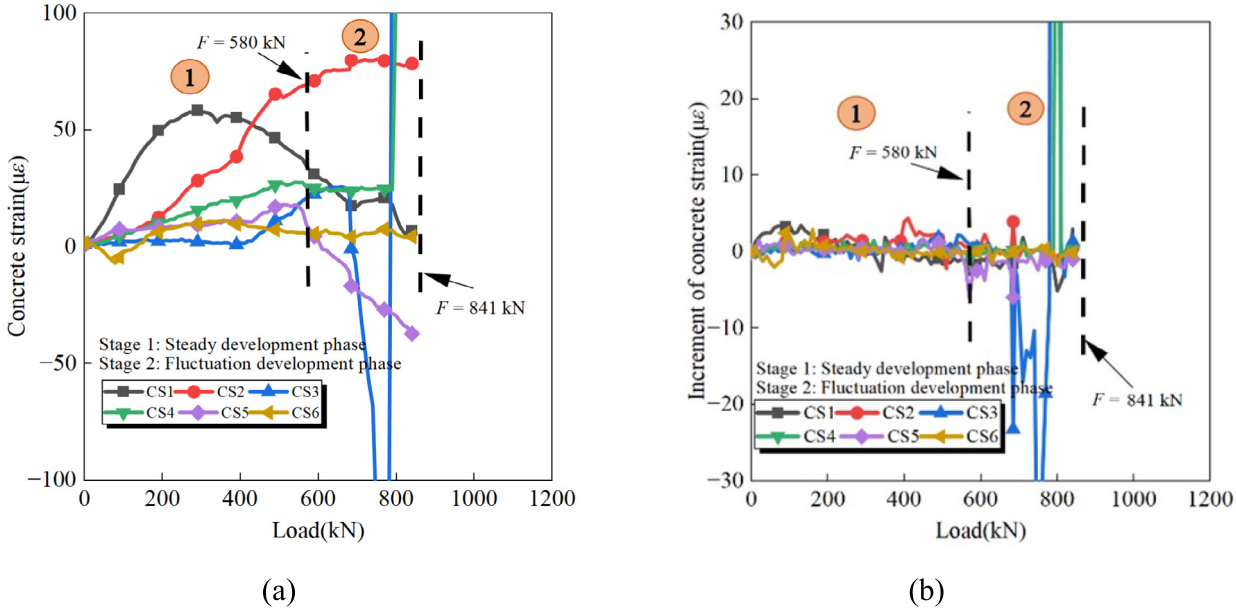

Fig. 15. Concrete strain properties of DRSJ in bottom face. (a) Load-concrete strain relationships, and (b) load-concrete strain increment relationships.

development phase, remaining close to zero. However, as the load increased beyond 1000 kN, the strain increments became more variable, reflecting the onset of fluctuations in concrete strain as the structure approached its load-bearing limit.

Moving to Fig. 14(a), the SRSJ also demonstrated a two-stage behavior in its load-concrete strain relationship. In the steady development phase, the strain increased slightly but remained controlled until the load reached around 800 kN. At this point, the strain began to increase more rapidly, and as the load progressed further into the fluctuation development phase, the strain showed significant fluctuations, particularly beyond 1085 kN. This behavior suggests that while SRSJ is capable of resisting strain initially, it becomes more susceptible to fluctuations as the load increases. Figure 14(b) supports this observation, showing that the concrete strain increments for SRSJ were minimal and stable in the steady development phase, but became increasingly erratic as the load entered the fluctuation development phase.

Figure 15(a) presents the load-concrete strain relationship for the DRSJ, which, like the previous joints, exhibited a two-stage behavior. However, the strain in DRSJ started to increase more significantly at a lower load level, around 580 kN. As the load approached 841 kN and entered the fluctuation development phase, the strain increased rapidly and showed larger fluctuations compared to CIJ and SRSJ. This indicates that DRSJ is less effective at controlling strain under increasing load, leading to more pronounced fluctuations. Figure 15(b) reveals that the concrete strain increments for DRSJ, while initially stable, became much larger and more erratic as the load increased beyond 580 kN, reflecting the joint's reduced ability to manage strain.

Overall, the CIJ is the most effective at maintaining stable concrete strain under load, with minimal fluctuations observed even at higher load levels. SRSJ, while initially stable, becomes more susceptible to strain fluctuations as the load increases, though it still manages to control strain better than DRSJ. DRSJ, on the other hand, showed significant strain increases and fluctuations at lower load levels, indicating a higher susceptibility to strain and reduced structural stability compared to CIJ and SRSJ. Furthermore, it is important to note that both SRSJ and DRSJ altered the stress distribution at the bottom surface compared to CIJ. While CIJ primarily subjected the bottom surface to tensile stress, SRSJ and DRSJ introduced areas where the bottom surface was in a compressive state. This change in stress mode is beneficial as it allows the concrete to better utilize its compressive strength.

3.5 Bolt strain

Figures 16–18 analyze the bolt strain behavior of CIJ, SRSJ, and DRSJ under increasing loads, focusing on the load–strain relationship and the strain increments (Cai et al., 2024a, 2024b). In Fig. 16(a), the CIJ bolts exhibited a steady increase in strain up to 520 kN, after which the strain began to fluctuate as the load approached 1116 kN. This behavior indicates that while CIJ bolts initially manage the load effectively, they become less stable as the load increases, especially at higher stress levels. Figure 16(b) confirms this by showing that the strain increments remained small and consistent in the early stages but became more erratic as the load increased.

For the SRSJ, as shown in Fig. 17(a), the strain grew steadily until around 580 kN, similar to the CIJ. However, beyond this point, the strain began to increase more rapidly

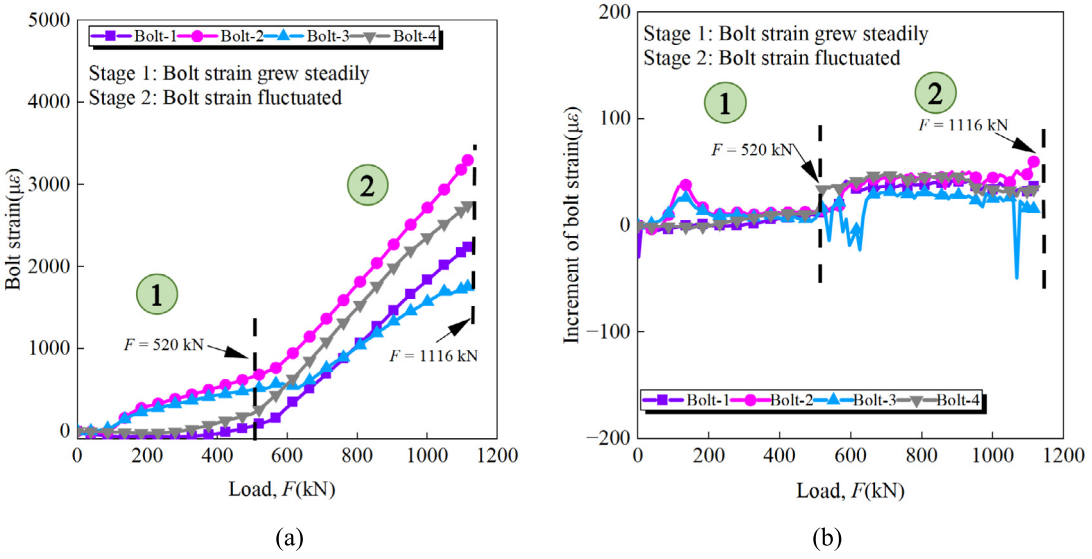

Fig. 16. Bolt strain properties of CIJ. (a) Load-bolt strain relationships, and (b) load-bolt strain increment relationships.

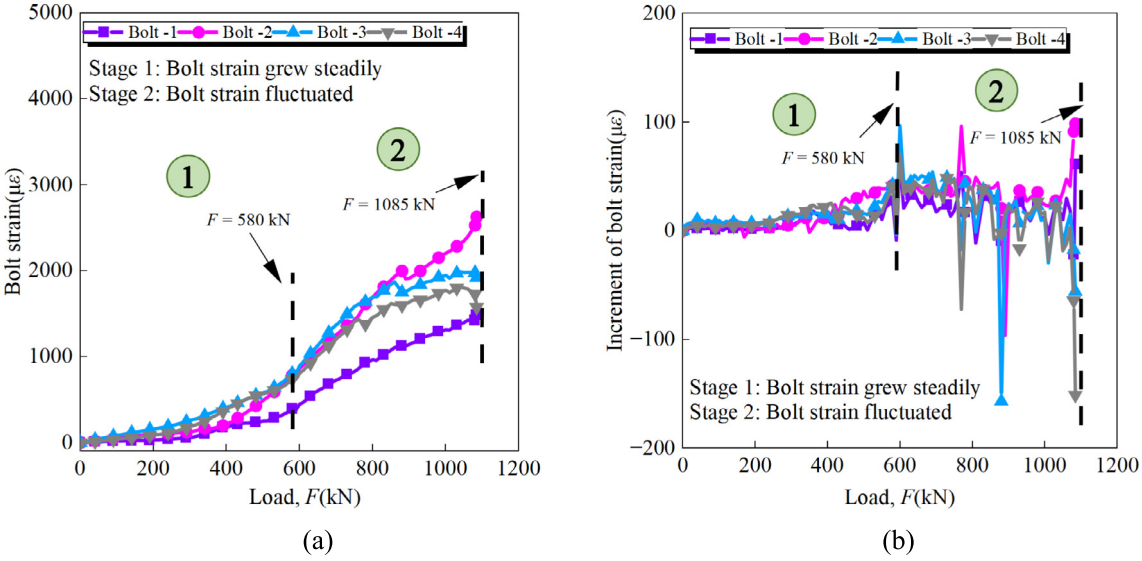

Fig. 17. Bolt strain properties of SRSJ. (a) Load-bolt strain relationships, and (b) load-bolt strain increment relationships.

and exhibited significant fluctuations as the load approached 1085 kN. This suggests that while SRSJ bolts handle initial loads well, they experience greater instability under higher loads. Figure 17(b) supports this, with strain increments showing a stable pattern initially but becoming more variable as the load increased, indicating a gradual decline in structural stability.

The DRSJ, depicted in Fig. 18(a), showed the most significant strain growth even at lower loads, with notable fluctuations starting around 290 kN and intensifying beyond 841 kN. This early onset of strain fluctuations suggests that DRSJ bolts are less capable of maintaining stability under load, leading to greater susceptibility to failure. Figure 18(b) further highlights this by showing larger and more erratic strain increments as the load increased, reflecting a significant decrease in stability under stress.

Overall, the CIJ bolts demonstrate better stability under load compared to SRSJ and DRSJ, which show increasing instability as the load rises. The DRSJ, in particular, exhibits the greatest strain and instability at lower loads, indicating a higher risk of structural compromise under stress.

Figure 19 presents the bolt strain properties, focusing on the average bolt strain (AVG) and the standard deviation (SD) across the different joint types: SRSJ, CIJ, and DRSJ. In Fig. 19(a), which illustrates the average bolt strain, the CIJ consistently exhibited the highest average strain across the load spectrum, particularly noticeable after 600 kN, where the strain increased sharply. The SRSJ, on the other hand, showed the lowest average strain throughout the

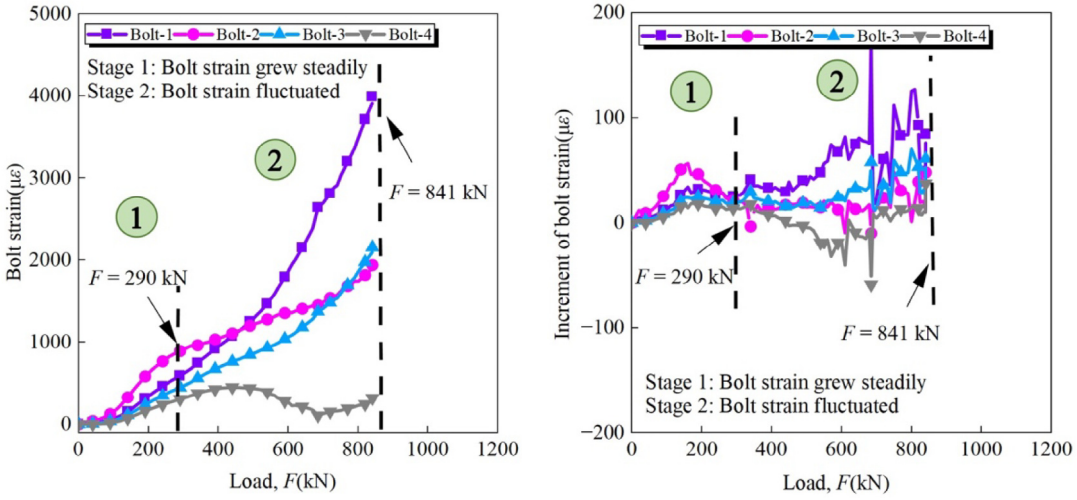

Fig. 18. Bolt strain properties of DRSJ. (a) Load-bolt strain relationships, and (b) load-bolt strain increment relationships.

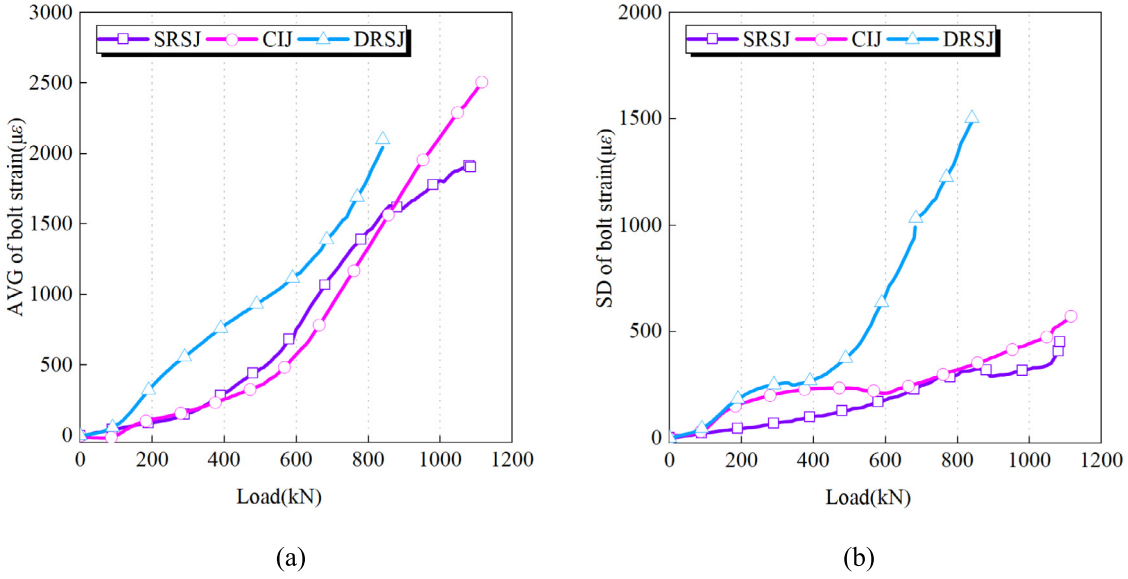

Fig. 19. Bolt strain properties. (a) Average bolt strain, and (b) standard deviation.

loading process, indicating that it experiences less deformation under the same load conditions. The DRSJ displayed an intermediate behavior, with average strain values higher than SRSJ but lower than CIJ, suggesting a moderate response to the applied load. Figure 19(b) focuses on the standard deviation of bolt strain, revealing insights into the variability and stability of the strain behavior under increasing loads. The CIJ demonstrated a relatively steady increase in standard deviation as the load increased, particularly beyond 600 kN, indicating more consistent but variable strain responses under high loads. In contrast, the DRSJ exhibited a significant rise in standard deviation starting from 600 kN, reflecting a higher variability and instability in its strain behavior as the load intensified. The SRSJ, maintaining the lowest standard deviation, indicated that it had the most stable and consistent strain response among the three joint types under the applied loads.

4 Discussions

4.1 Joint toughness

Table 2 presents the toughness indices of three joint types across different load phases: the elastic phase, plastic stable phase, and plastic accelerated phase. The toughness index, defined as the area under the load–deflection curve up to the end of each phase, reflects the energy absorption

Table 2
Joint toughness index.

Phase	Toughness (kN•mm)		
	CIJ	SRSJ	DRSJ
Elastic phase	230	336	268
Plastic stable phase	3283	6259	3536
Plastic accelerated phase	14 201	20 047	9527

capacity of each joint during these phases. Higher values indicate greater toughness, meaning a greater ability to absorb energy under loading conditions (Cai et al., 2024a, 2024b; Gong et al., 2017).

In the elastic phase, the SRSJ shows the highest toughness at 336 kN•mm, which is approximately 46.1% higher than the CIJ's 230 kN•mm and 25.4% higher than the DRSJ's 268 kN•mm. This indicates that SRSJ has the best ability to absorb energy in the initial, elastic stage of loading. The DRSJ also outperforms the CIJ by about 16.5%, demonstrating a slightly better energy absorption capacity during this phase. In the plastic stable phase, the toughness of the SRSJ significantly surpasses that of the other joints, reaching 6259 kN•mm. This is an increase of 90.7% compared to the CIJ's 3283 kN•mm, showing that the SRSJ can absorb nearly twice the energy during this phase. The DRSJ, with a toughness of 3536 kN•mm, is only 7.7% higher than the CIJ, indicating a marginal improvement over the traditional joint. The most significant differences are observed in the plastic accelerated phase. Here, the SRSJ again leads with a toughness of 20 047 kN•mm, which is 41.2% higher than the DRSJ's 9527 kN•mm and a remarkable 41.2% higher than the CIJ's 14 201 kN•mm. The DRSJ, while improving on the CIJ in earlier phases, falls behind in this critical phase by 32.9% compared to SRSJ, indicating its lower capacity to absorb energy as the load increases rapidly.

Overall, the SRSJ consistently exhibits superior toughness across all phases, particularly in the plastic stable and plastic accelerated phases, where its energy absorption capacity is nearly double that of the CIJ. The DRSJ, while showing some improvements over the CIJ in earlier phases, fails to match the toughness of the SRSJ, particularly in the later stages of loading.

4.2 Joint ductility

Table 3 presents the ductility indices for the three joint types, focusing on both deflection and rotational angle ductility coefficients. The joint ductility coefficients were defined based on the ratio of maximum deformation in the plastic stable phase to the maximum deformation in the elastic phase, as measured by deflection and rotational angle (Cai et al., 2024a, 2024b; Gong et al., 2017).

For the deflection ductility coefficient (μ_δ), the RCS joint showed the highest coefficient of 4.44. This indicates that RCS is the most ductile in terms of deflection among the three joints. The SRSJ joint had a slightly lower coefficient of 4.31, which is approximately 2.9% less than the RCS, indicating a comparable level of deflection ductility. In contrast, the DRSJ joint had the lowest deflection ductility coefficient of 3.50, which is about 21.2% lower than the RCS, suggesting that it has the least ability to accommodate deflection. For the rotational angle ductility coefficient (μ_θ), the SRSJ joint exhibited the highest value at 7.63, indicating a significant rotational flexibility. This is 76.4% higher than the RCS's coefficient of 4.32, showcasing the SRSJ's superior ability to undergo rotational deformation. The RCS joint, with a coefficient of 4.32, reflects a balanced rotational ductility. Meanwhile, the DRSJ joint, with the lowest coefficient of 3.43, is approximately 20.6% lower than the RCS, indicating its limited capacity to handle rotational deformation.

While the RCS joint leads in deflection ductility, the SRSJ joint surpasses both RCS and DRSJ in rotational ductility, making it particularly strong in handling rotational movements. The DRSJ joint, however, falls behind in both categories, suggesting limitations in both deflection and rotational flexibility.

4.3 Cracking pattern

The cracking patterns observed in the concrete joints, as depicted in Figs. 20–22, reveal critical insights into the structural performance and failure modes of the CIJ, SRSJ, and DRSJ, respectively. These patterns are indicative of the underlying stress distribution and the joints' ability to withstand applied loads before failure.

Table 3
Joint ductility index.

Parameter	Explanation	Unit	RCS	SRSJ	DRSJ
δ_{cr}	Maximum deflection in the elastic growth phase	mm	1.90	2.69	2.91
δ_{psp}	Maximum deflection in the plastic stable phase	mm	8.44	11.69	10.20
μ_δ	Deflection ductility coefficient (δ_{psp}/δ_{cr})	–	4.44	4.31	3.50
θ_{cr}	Maximum rotational angle in the elastic growth phase	10^{-3} rad	2.89	2.03	4.31
θ_{psp}	Maximum rotational angle in the plastic stable phase	10^{-3} rad	12.49	15.49	14.80
μ_θ	Rotational angle ductility coefficient (θ_{psp}/θ_{cr})	–	4.32	7.63	3.43

Fig. 20. Cracking pattern of CIJ.

Fig. 21. Cracking pattern of SRSJ.

Fig. 22. Cracking pattern of DRSJ.

Figure 20, showing the cracking pattern of CIJ, reveals a relatively uniform distribution of cracks, indicative of the joint's robust but brittle behavior under load. The cracks primarily originated from the bottom surface, propagating upwards due to tensile stresses. Additionally, a significant observation in CIJ is the severe spalling on the top surface, where concrete crushing has led to large-scale material loss and exposed rebar. This suggests that while the CIJ is effective in delaying failure through a balanced load transfer, the upper surface is vulnerable to compressive forces, leading to extensive damage as the load increases. The side surfaces of the CIJ also showed significant cracking, particularly originating from the tensile zone. This is likely due to the hand hole structure, which tends to concentrate tensile stresses around it, making it a weak point under load. Furthermore, the high-strength bolts in the CIJ exhibited localized twisting deformation, contributing to the overall stress concentration and further compromising the joint's ability to maintain structural integrity under high load conditions.

Figure 21 illustrates the cracking pattern of SRSJ, where the damage is more localized compared to CIJ. The cracks are concentrated around the joint area, with more pronounced cracking at the bottom surface, which eventually exposes the joint itself as the concrete fractures. Unlike the CIJ, the top surface of the SRSJ exhibited only minor spalling, suggesting that the joint is better at managing compressive forces on the upper surface. However, the exposure of the joint at the bottom surface indicates that while SRSJ can handle deformation, it may be at the expense of compromising the joint's protective concrete cover. The side surfaces of the SRSJ showed cracks mainly in the compression zone, indicating a different stress distribution compared to CIJ. The limited spalling on the top surface reflects SRSJ's ability to maintain structural integrity, but the concentration of cracks around the joint area highlights a potential risk for localized failure. Similar to CIJ, the high-strength bolts in the SRSJ also showed signs of localized twisting deformation, particularly as the joint approached its load-bearing limits, which may have exacerbated the cracking patterns observed.

In contrast, Fig. 22 shows the cracking pattern of DRSJ, which exhibited the most complex and severe damage among the three joints. The DRSJ's dual-row sleeve design appears to contribute to significant stress concentrations, particularly at the bottom surface, leading to extensive and irregular cracking. Interestingly, despite these severe cracks at the bottom, the top surface of the DRSJ showed

no significant concrete cracking or spalling. This lack of top surface damage suggests that the DRSJ's design effectively shields the upper concrete from compressive forces. However, the severe stress concentrations and the corresponding cracking pattern at the bottom indicate that the DRSJ struggles to distribute the load evenly across the joint, leading to a lower load-bearing capacity and a more brittle failure mode. The side surfaces of the DRSJ also exhibited cracks primarily in the compression zone, similar to SRSJ, suggesting that the dual-row design does not effectively mitigate stress concentrations in these areas. The high-strength bolts in the DRSJ also experienced localized twisting deformation, which, combined with the stress concentration, likely contributed to the earlier and more severe failure observed in this joint.

4.4 Sustainability

The sustainability indicator is determined by analyzing the embodied carbon (EC) and cost values. After a comprehensive market study (Cai et al., 2024c; Ye et al., 2023), the EC and costs for each raw material are detailed in Table 4. Figure 23 showcases the embodied carbon (EC) and costs for a standard 1/8 segment of a tunnel ring with an outer diameter of 9 m and an inner diameter of 8.3 m. The CIJ exhibited the highest embodied carbon, followed by the SRSJ and DRSJ. This higher embodied carbon for the CIJ is primarily due to its significant use of iron and cement, which have substantial carbon footprints. In contrast, the SRSJ and DRSJ, with more efficient material use, demonstrate lower embodied carbon values. Specifically, the SRSJ achieved a reduction of approximately 7.21% in embodied carbon compared to the CIJ, while the DRSJ showed an even greater reduction of 7.48%. In terms of cost, the CIJ was again the highest, followed by the SRSJ and DRSJ. The SRSJ and DRSJ designs, which optimize material usage, resulted in a cost reduction compared to the CIJ. The SRSJ showed a cost reduction of about 6.42%, and the DRSJ achieved a 6.68% reduction compared to the CIJ. These reductions illustrate the economic efficiency of the sleeve joint designs.

Table 4
Breakdown of embodied carbon and cost of raw materials.

Raw materials	Embodied carbon (kg/kg)	Cost ($/kg)
Cement	0.912	0.044
Water	0.001	0.000 53
Fly ash	0.004	0.024
Slag	0.042	0.27
Fine sand	0.005	0.058
Coarse aggregate	0.005	0.058
Admixture	1.88	2.98
Iron	1.29	0.4653

The proportions of embodied carbon and cost for the CIJ, SRSJ, and DRSJ, as presented in Figs. 24 and 25, provide further insights into the environmental and economic efficiencies of these joint types. The proportions of embodied carbon reveal that cement is the primary contributor across all joint types, accounting for around 50.79% in CIJ, and slightly higher in SRSJ (54.99%) and DRSJ (55.17%). This indicates that the use of cement remains a significant factor in the environmental impact of these joints, with SRSJ and DRSJ marginally increasing their reliance on cement compared to CIJ. The steel cage also contributes substantially, with proportions of 23.96% in CIJ, increasing slightly in SRSJ (25.82%) and DRSJ (25.90%). The joint material itself contributes a notable proportion in CIJ at 21.74%, but this is reduced in the SRSJ (15.38%) and DRSJ (15.12%), reflecting the more efficient material usage in the sleeve joints. In terms of cost proportions, coarse aggregate and fine sand represent the largest cost factors across all joints. The CIJ sees 24.54% of its cost attributed to coarse aggregate, with SRSJ (26.35%) and DRSJ (26.42%) showing slightly higher proportions, aligning with their increased efficiency in material use. The cost associated with the joint material itself is significantly higher in CIJ (19.50%) compared to SRSJ

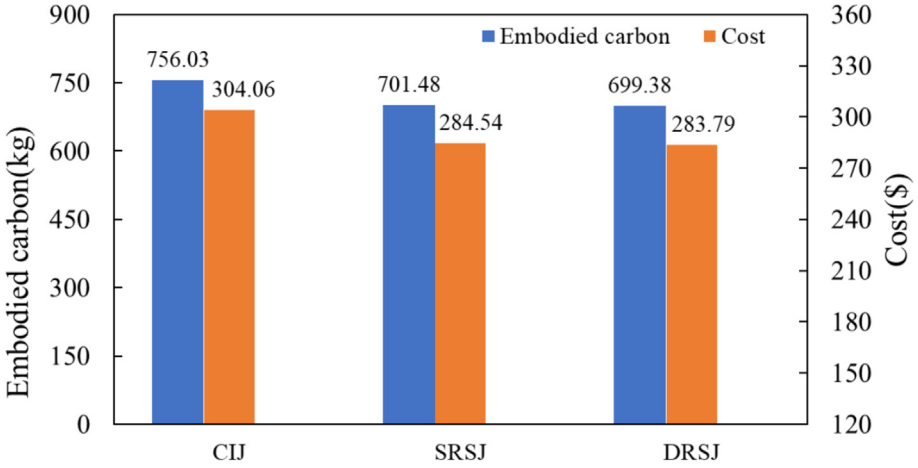

Fig. 23. Embodied carbon and cost of different segmental joints.

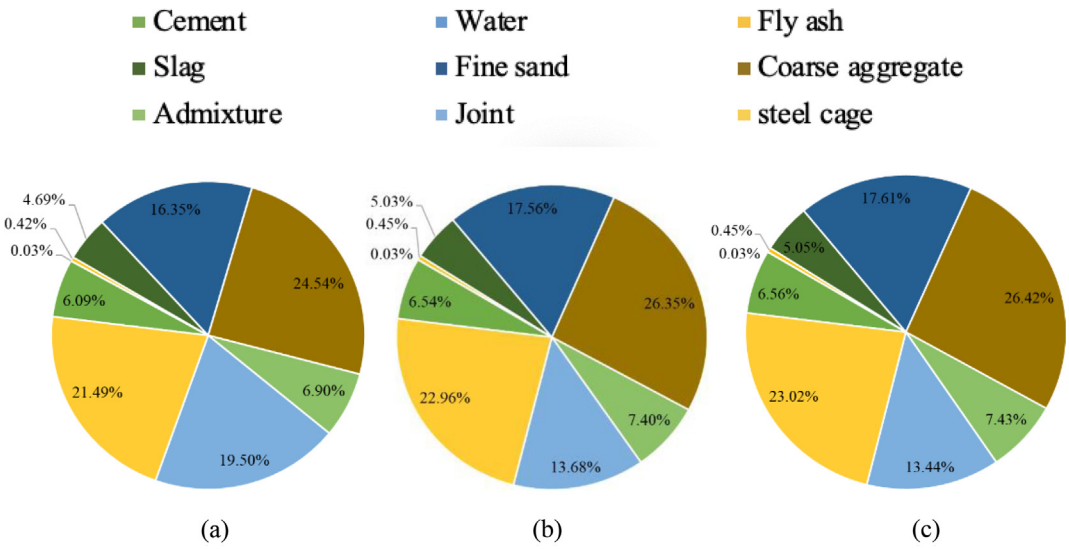

Fig. 24. Embodied carbon proportion. (a) CIJ, (b) SRSJ, and (c) DRSJ.

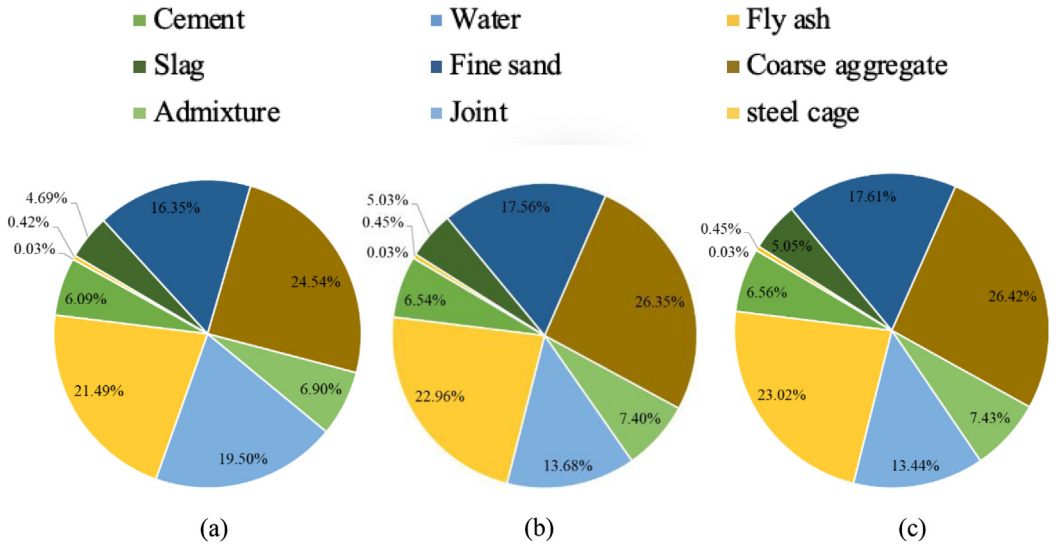

Fig. 25. Cost proportion. (a) CIJ, (b) SRSJ, and (c) DRSJ.

(13.68%) and DRSJ (13.44%), again highlighting the material efficiency of the sleeve joints. The cost proportions for the steel cage also increase from 21.49% in CIJ to 22.96% in SRSJ and 23.02% in DRSJ, reflecting the slightly higher steel usage in these designs.

DRSJ and SRSJ emerge as more sustainable and cost-effective alternatives compared to the traditional CIJ, primarily due to their optimized material usage, which results in lower embodied carbon and costs. However, when considering structural load-bearing performance, the SRSJ stands out as the best option, achieving 97.22% of the load-bearing capacity of the CIJ, making it the optimal choice in terms of both sustainability and structural performance.

5 Conclusions

This study was conducted in response to the growing need for optimizing shield tunnel joints, considering the increasing emphasis on structural performance, low-carbon emissions, and economic efficiency in modern construction. While CIJ has been the traditional solution, it is associated with high material costs and significant environmental impact due to its heavy reliance on iron. To address these issues, this research explored two alternative joint designs: SRSJ and DRSJ, focusing on their mechanical performance and sustainability metrics. The research methods involved extensive experimental testing focusing on joint deflection, joint opening, rotational angle, concrete strain,

and bolt strain. Additionally, the study analyzed key performance aspects such as joint toughness, ductility, cracking patterns, and sustainability to provide a comprehensive evaluation of the three joint types. Key insights include:

(1) The SRSJ demonstrated a load-bearing capacity close to CIJ, reaching 97%, while the DRSJ performed significantly lower, achieving only 75% of CIJ's capacity. In the elastic phase, SRSJ exhibited superior load-bearing performance, supporting twice the load of CIJ, with DRSJ showing 1.23 times the capacity. This advantage stems from the different stress distribution patterns in the joints, where SRSJ and DRSJ combined tension and compression forces more effectively than CIJ.
(2) Bolt strain analysis revealed that DRSJ bolts experienced the highest stress levels and the most variability, indicating stress concentration issues. In contrast, SRSJ showed behavior similar to CIJ, maintaining a balanced stress distribution.
(3) SRSJ outperformed both CIJ and DRSJ in toughness and ductility, especially in rotational flexibility, where it exceeded CIJ by over 76%. This superior toughness allows SRSJ to absorb more energy and sustain deformation without failure.
(4) CIJ suffered from significant spalling and cracking under load, while SRSJ localized damage around the joint and minimized top surface spalling. DRSJ, however, exhibited the most severe damage, with extensive bottom surface cracking.
(5) SRSJ and DRSJ reduced embodied carbon and costs by optimizing material usage, achieving reductions of 7.21% and 7.48% in carbon emissions and 6.42% and 6.68% in cost, respectively, compared to CIJ.
(6) SRSJ proved to be a strong alternative to CIJ, offering a balanced combination of mechanical performance, sustainability, and cost efficiency. On the other hand, DRSJ, despite its larger contact area, struggled with stress concentration issues, leading to reduced structural effectiveness and lower overall advantages.

This study examined the characteristics of three types of joints under static load conditions. Future research can focus on the long-term performance of these joints under different environmental factors, such as temperature changes and exposure to moisture. This will provide important data for optimizing joint designs in real-world applications, especially for tunnels in diverse and challenging conditions.

Data availability

The data that support the findings of this study are available from the corresponding author upon reasonable request.

CRediT authorship contribution statement

Minjin Cai: Methodology, Data curation, Software, Writing – original draft, Resources, Validation, Conceptualization. **Timon Rabczuk:** Supervision, Conceptualization, Methodology. **Shuwei Zhou:** Methodology, Conceptualization, Supervision. **Xiaoying Zhuang:** Resources, Supervision, Validation, Methodology, Conceptualization, Funding acquisition, Writing – review & editing.

Declaration of competing interest

Dr. Timon Rabczuk is an associate editor for *Underground Space* and was not involved in the editorial review or the decision to publish this article. All authors declare that there are no competing interests.

Acknowledgement

The authors gratefully acknowledge the support from the National Natural Science Foundation of China (Grant No. 52278411) and Shanghai Science and Technology Innovation Action (22JC14041001).

References

Alani, A. H., Tayeh, B. A., Johari, M. A. M., & Majid, T. (2024). Optimizing strength behavior of sustainable ultra high performance green concrete with minimum cement content using response surface method. *Journal of Building Pathology and Rehabilitation, 9*, 110.

Al-Mansour, A., Chow, C. L., Feo, L., Penna, R., & Lau, D. (2019). Green concrete: By-products utilization and advanced approaches. *Sustainability, 11*(19), 5145.

Assaad, R. H. (2024). Examining low-carbon material initiatives: Existing policies, impacts on the procurement of projects, current challenges, and potential solutions to reduce embodied carbon in the construction industry. *Journal of Legal Affairs and Dispute Resolution in Engineering and Construction, 16*(2), 04523060.

Cai, M., Zhu, H., Chen, Q., Rabczuk, T., & Zhuang, X. (2024a). Mechanical behavior of ultra-high toughness concrete (UHTC) tunnel segmental joints. *Tunnelling and Underground Space Technology, 151*, 105838.

Cai, M., Zhu, H., Chen, Q., Rabczuk, T., & Zhuang, X. (2024b). Performance of Engineered Cementitious Composites (ECC) in shield tunnel segmental joints: A comparative study with ordinary reinforced concrete. *Case Studies in Construction Materials, 20*, e03138.

Cai, M., Zhu, H., Wan, Y., Zhu, H., Rabczuk, T., & Zhuang, X. (2024c). Using ultrafine fly ash to achieve low-carbon, high strength and high toughness engineered cementitious composites LC-HSTC. *Case Studies in Construction Materials, 20*, e03259.

Chen, L., Huang, Z., Pan, W., Su, R. K., Zhong, Y., & Zhang, Y. (2024). Low carbon concrete for prefabricated modular construction in circular economy: An integrated approach towards sustainability, durability, cost, and mechanical performances. *Journal of Building Engineering, 90*, 109368.

Cheng, L., Jin, H., Liu, J., & Xing, F. (2024). A comprehensive assessment of green concrete incorporated with municipal solid waste incineration bottom: Experiments and life cycle assessment (LCA). *Construction and Building Materials, 413*, 134822.

Deutscher Ausschuss für unterirdisches Bauen e. V. (DAUB). (2013). *Recommendations for the design, production and installation of segmental rings* (Technical report).

Gong, C., Ding, W., Mosalam, K. M., Günay, S., & Soga, K. (2017). Comparison of the structural behavior of reinforced concrete and steel fiber reinforced concrete tunnel segmental joints. *Tunnelling and Underground Space Technology, 68*, 38–57.

Li, Z., Soga, K., Wang, F., Wright, P., & Tsuno, K. (2014). Behaviour of cast-iron tunnel segmental joint from the 3D FE analyses and development of a new bolt-spring model. *Tunnelling and Underground Space Technology, 41*, 176–192.

Liew, K., Sojobi, A., & Zhang, L. (2017). Green concrete: Prospects and challenges. *Construction and Building Materials, 156*, 1063–1095.

Lombardi, M., Berardi, D., Galuppi, M., & Barbieri, M. (2023). Green tunnel solutions: An overview of sustainability trends in the last decade (2013–2022). *Buildings, 13*(2), 392.

López, A. R., Tsiampousi, A., Standing, J. R., & Potts, D. M. (2023). Numerical characterisation of the rotational behaviour of grey cast iron tunnel joints. *Computers and Geotechnics, 159*, 105460.

Marques, E. S., Silva, F., Paiva, O. C., & Pereira, A. B. (2019). Improving the mechanical strength of ductile cast iron welded joints using different heat treatments. *Materials, 12*(14), 2263.

Migunthanna, J., Rajeev, P., & Sanjayan, J. (2024). Flexural fatigue performance of pavement-grade low-carbon concrete containing waste clay bricks. *Journal of Materials in Civil Engineering, 36*(11), 04024386.

Ouyang, Z., Zheng, H., Naito, C., Quiel, S., & Mooney, M. (2024). Testing of axial-moment-rotation response for skewed flat radial joints in precast concrete segmental tunnel linings. *Tunnelling and Underground Space Technology, 150*, 105812.

Rodríguez, R., & Pérez, F. (2021). Carbon foot print evaluation in tunneling construction using conventional methods. *Tunnelling and Underground Space Technology, 108*, 103704.

Saleh, A., Saleh, N., Ali, O., Hasan, R., Ahmed, O., Alias, A., & Yassin, K. (2024). Green building techniques: under the umbrella of the climate framework agreement. *Babylonian Journal of Machine Learning, 2024*, 1–14.

Sivakrishna, A., Adesina, A., Awoyera, P., & Kumar, K. R. (2020). Green concrete: A review of recent developments. *Materials Today: Proceedings, 27*, 54–58.

Song, Y., Zhu, H., Shen, Y., & Feng, S. (2024). Green tunnel lighting environment: A systematic review on energy saving, visual comfort and low carbon. *Tunnelling and Underground Space Technology, 144*, 105535.

Tsiampousi, A., Yu, J., Standing, J., Vollum, R., & Potts, D. (2017). Behaviour of bolted cast iron joints. *Tunnelling and Underground Space Technology, 68*, 113–129.

Ünal, M. T., Bin Hashim, H., Gökçe, H. S., Ayough, P., Köksal, F., El-Shafie, A., Şimşek, O., & Pordesari, A. (2024). Development and characterization of basalt fiber-reinforced green concrete utilizing coconut shell aggregates. *Sustainability, 16*(17), 7306.

Xu, H., Liu, Q., Li, B., & Guo, C. (2024). Identification of shield tunnel segment joint opening based on annular seam pressure monitoring. *Sensors, 24*(12), 3924.

Ye, J., Teng, F., Yu, J., Yu, S., Du, H., Zhang, D., Ruan, S., & Weng, Y. (2023). Development of 3D printable engineered cementitious composites with incineration bottom ash (IBA) for sustainable and digital construction. *Journal of Cleaner Production, 422*, 138639.

Zhang, C., Zhao, Z., Xu, Y., & Nie, X. (2024c). Study on the shear mechanical response and failure characteristics of prefabricated double-cabin utility tunnel joints. *Journal of Civil Structural Health Monitoring, 14*(7), 1595–1610.

Zhang, J., Shi, P., Huang, J., Li, H., & Zhou, X. (2018). Green tunnel construction technology and application. *IOP Conference Series: Earth and Environmental Science, 153*, 052052.

Zhang, Y., Saadat, Y., Huang, H., Zhang, D., & Ayyub, B. M. (2024d). Experimental study on deformational resilience of longitudinal joint in shield tunnel lining. *Structure and Infrastructure Engineering, 20*(3), 368–379.

Zhang, Z., Li, A., & Zhang, Z. (2024a). Recent advances in durability improvement and low-carbon strategy of engineering materials and structures. *Frontiers in Materials, 11*, 1407364.

Zhang, Z., Zheng, G., Cheng, X., Liang, R., Li, C., Zhong, Z., & Zhao, J. (2024b). Analytical approach for longitudinal deformation of shield tunnels considering bending-shear-torsional effects of circumferential joints. *Tunnelling and Underground Space Technology, 152*, 105946.